Supporting Information to:

Cross Conjugation in Polyenes and Related Hydrocarbons: What Can Be Learned from Valence Bond Theory about Single-Molecule Conductance?

Junjing Gu[a], Wei Wu*[a], Thijs Stuyver*[b,c], David Danovich[b], Roald Hoffmann*[d], Yuta Tsuji[e], and Sason Shaik*[b]

a. State Key Laboratory of Physical Chemistry of Solid Surfaces, *i*ChEM, Fujian Provincial Key Laboratory of Theoretical and Computational Chemistry and College of Chemistry and Chemical Engineering, Xiamen University, Xiamen, Fujian 361005, China

b. Department of Organic Chemistry and the Lise Meitner-Minerva Centre for Computational Quantum Chemistry, The Hebrew University, Jerusalem 91904, Israel

c. Algemene Chemie, Vrije Universiteit Brussel, Pleinlaan 2, 1050 Brussels, Belgium

d. Department of Chemistry and Chemical Biology, Cornell University, Baker Laboratory, Ithaca NY 14853

e. Institute for Materials Chemistry and Engineering and IRCCS, Kyushu University, Nishi-ku, Fukuoka 819-0395, Japan

I. Geometries of linear polyenes, dendralenes, *o*-quidimethanes (*o*-QDM) and *p*-quinodimethanes (*p*-QDM)

I.A Dendralenes

The smallest [3]dendralene C_6H_8 was optimized using B3LYP/D95V, B3LYP/cc-aug-pVTZ, MP2/D95V and MP2/aug-cc-pVTZ. All the methods produced a skewed structure, in accord with experimental electron diffraction data.[S1] Table S1 includes all these details.

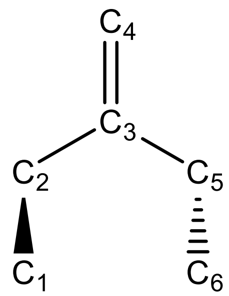

Scheme S1. The skeletons of cross-conjugated C_6H_8 [dendralene].

Table S1. The geometrical parameters of planar and skew C_6H_8[a].

C_6H_8	ED[b]	planar B3LYP/ D95V	planar MP2/ D95V	planar B3LYP/ ACT	planar MP2/ ACT	skew B3LYP/ D95V	skew MP2/ D95V	skew B3LYP/ ACT[c]
r(C3=C4)	1.350	1.368	1.385	1.348	1.354	1.365	1.365	1.345
r(C1=C2)	1.342	1.354	1.373	1.333	1.342	1.354	1.372	1.333
r(C5=C6)	1.342	1.354	1.373	1.333	1.342	1.354	1.372	1.333
r(C2-C3)	1.479	1.484	1.503	1.471	1.467	1.485	1.504	1.472
r(C3-C5)	1.479	1.484	1.503	1.471	1.467	1.485	1.504	1.472
θ(C2-C3-C5)	119.6	126.4	126.4	126.4	126.8	123.2	121.6	123.2
φ(C2-C3=C4-C5)	0.00	0.00	0.00	0.00	0.00	0.00	0.00	0.00
φ(C1=C2-C5=C6)	39.3	0.00	0.00	0.00	0.00	34.8	43.3	35.3

[a] bond length in Å and angle in degree; [b] *Acta Chemica Scandinavica A*, **1988**, *42*, 634-650. [c] aug-cc-pVTZ

As can be seen from Table S1, the lengths of both double and single bonds of planar

C_6H_8 at B3LYP/D95V and MP2/D95V levels are longer than the ED data for the skewed structure. The C3=C4 at MP2/aug-cc-pVTZ level is slightly longer than experimental result. Note however that the geometrical parameters of planar C_6H_8 at B3LYP/aug-cc-pVTZ level are very close to the ED data for the skewed conformer.

I.A.1. Can planar dendralene serve as a model?

To answer the question, both planar and skew C_6H_8 were optimized at B3LYP/D95V level and the following CASSCF and VBSCF calculations are at D95V level with the same active electrons and orbitals. Both σ and π orbitals are optimized in VBSCF calculations.

Table S2. Comparison of the weight W(R(0))[a] between planar and skew cross-conjugated C_6H_8 at VBSCF(HAO)/D95V and VBSCF(BDO)/D95V levels.

	W(R(0))(planar)		W(R(0))(skew)	
	HAO	BDO	HAO	BDO
C_6H_8	0.787	0.777	0.816	0.797

[a] The weight of the fundamental Lewis structure.

Table S3. The delocalization energy[a] (unit in kcal mol^{-1}) for planar and skewed cross-conjugated C_6H_8 at VBSCF/D95V level with both HAO and BDO.

		E(Full)[b]	E(R(0))[b]	$\Delta E_{\text{del-VBSCF}}$
C_6H_8(planar)	HAO	-231.706	-231.698	4.6
	BDO	-231.808	-231.790	11.7
C_6H_8(skew)	HAO	-231.710	-231.704	3.6
	BDO	-231.812	-231.795	10.5

[a] $\Delta E_{del-VBSCF} = E(Full) - E(R(0))$. [b] HAOs are hybrid atomic orbitals, while BDOs are bond-distorted orbitals.
[b] in a.u.

Table S4. Delocalization energy (in kcal mol^{-1})^{a} for planar and skew cross-conjugated C_6H_8 at VBSCF/D95V level with both HAO and BDO.

Structure		$\Delta E_{del\text{-}CASSCF}$
C_6H_8(planar)	HAO	76.4
	BDO	18.9
C_6H_8(skew)	HAO	74.7
	BDO	17.5

^{a} $\Delta E_{del-CASSCF} = E(R(0)) - E(CAS(6,6))$. ^{b} The terms HAO and BDO refer to the VBSCF wave function of R(0).

The conclusion from Tables S2-S3 is that VBSCF and CASSCF calculations show that the skewed conformation of [3]dendralene is less delocalized compared with the planar conformer**.** In this sense, the planar dendralene can serve as a safe limiting model, with an upper extent of delocalization, for the actual skewed dendralene.

I.A.2. Why is the skewed form of [3]dendralene more stable than the planar?

We note that the angle C2C3C5 in planar C_6H_8 (126.4°) is larger than that in skewed conformer [123.2°] (see Scheme S2). To understand the reason, we optimized all other parameters of the planar conformer with a fixed angle C2C3C5, which is the same as the one in the skewed conformer, and got the distortion energy in Table S5.

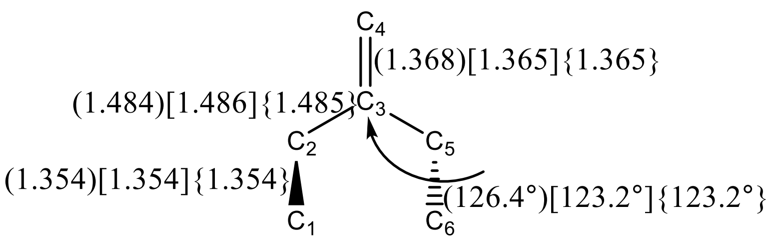

Scheme S2. The key geometrical parameters for planar, planar$_{dis}$ and skew C_6H_8^{a}.

^{a} data in (), [] and {} are for planar, planar$_{dis}$ and skew C_6H_8 respectively.

Table S5. The distortion energy ΔE_{dis}[a] (unit in kcal mol^{-1}) between planar and planar$_{dis}$ C_6H_8 at B3LYP/D95V level.

E(planar$_{dis}$)[b]	E(planar)[b]	ΔE_{dis}
-233.352	-233.353	0.4

[a] $\Delta E_{dis} = E(planar_{dis}) - E(planar)$

[b] in a.u.

The distortion energy calculated, with respect to the C-C-C angle opening, is too small to account for the preference of C_6H_8 for a skewed conformation. In Table S3 we see that R(0) prefers a skewed conformation by 3.3 kcal/mol, and the full VBSCF state prefers the skewed conformer by 2.1 kcal/mol. This means that the fundamental VB structure, R(0), determines the skewing preference, due to $\pi-\pi$ Pauli repulsion, while the difference of ~1.2 kcal/mol between skewed and planar, might reflect steric repulsion of the H---H on C1 and C6.]

In the GKS-EDA method,[S2] the total interaction energy is decomposed into electrostatic, exchange, repulsion, polarization, and correlation terms. Using this method (Table S6), we found that the H---H repulsion in the planar conformation is reduced at the skewed conformation by ~1.6 kcal/mol, which is close to the above estimate of ~1.2 kcal/mol.

Table S6. The interaction energy ΔE[a] (unit in kcal mol^{-1}) between the H---H on C1 and C6 in C_6H_8 at B3LYP/D95V level.

H---H	$\Delta E^{\mathrm{frozen}}$	ΔE^{pol}	ΔE^{corr}	ΔE
planar	7.9	-6.5	2.1	3.5
skew	2.6	-2.5	1.8	1.9

[a] Ref. S2, $\Delta E^{\mathrm{frozen}} = \Delta E^{ele} + \Delta E^{ex} + \Delta E^{rep}$

I.A.3. Will the geometrical differences, of different levels, affect the VB results?

To answer this question, we carried out VBSCF calculations on the B3LYP geometries, obtained with D95V and aug-cc-pVTZ.

a) Geometry optimization: B3LYP/D95V

VB calculation: VBSCF/D95V with only π optimization

Table S7. The weight W(R(0)) for planar C_6H_8 at VBSCF(HAO)/D95V VBSCF(BDO)/D95V levels.

	HAO	BDO
W(R(0))	0.787	0.777

Table S8. The delocalization energy[a] ($\Delta E_{del\text{-}VBSCF}$, unit in kcal mol^{-1}) for planar C_6H_8 at VBSCF/D95V level with both HAO and BDO.

	E(R(0))	E(Full)	$\Delta E_{del\text{-}VBSCF}$
HAO	-231.7	-231.7	4.6
BDO	-231.8	-231.8	11.8

[a]$\Delta E_{del\text{-}vbscf} = E_{R(0)} - E_{VB,full}$

Table S9. Delocalization energy ($\Delta E_{del\text{-}CASSCF}$, unit in kcal mol^{-1})[a] for planar C_6H_8 at VBSCF/D95V level with both HAO and BDO.

	HAO	BDO
$\Delta E_{del\text{-}CASSCF}$	76.5	19.2

[a]$\Delta E_{del\text{-}casscf(} = E_{R(0)} – E_{CAS(6,6)}$

b) Geometry optimization: B3LYP/aug-cc-pVTZ

VB calculation: VBSCF/D95V with only π optimization

Table 10. The weight W(R(0)) for planar C_6H_8 at VBSCF(HAO)/D95V and VBSCF(BDO)/D95V levels.

	HAO	BDO
W(R(0))	0.793	0.781

Table S11. The delocalization energy ($\Delta E_{del\text{-}VBSCF}$, unit in kcal mol^{-1}) for planar C_6H_8 at VBSCF/D95V level with both HAO and BDO.

	E(R(0))	E(Full)	$\Delta E_{del\text{-}VBSCF}$
HAO	-231.7	-231.7	4.5
BDO	-231.8	-231.8	11.9

Table S12. Delocalization energy ($\Delta E_{del\text{-}CASSCF}$, unit in kcal mol^{-1}) for planar C_6H_8 at CASSCF/D95V level with both HAO and BDO.

	HAO	BDO
$\Delta E_{del\text{-}CASSCF}$	79.1	19.5

Conclusion: As seen from the above Tables, irrespective of the difference in the optimized geometries of the planar and skewed conformations, we are getting nearly the same W(*R*(0)), and delocalization energy for planar C_6H_8. So we can do VBSCF calculations based on the geometries optimized at B3LYP/D95V level.

I.A.4. Comparison of geometric features for cross-conjugated and linear polyenes

Figure 7 in the main text shows the B3LYP/D95V optimized geometries for $C_{2n}H_{2n+2}$ (n = 2-8) cross-conjugated and linear polyenes. Here in Scheme S3 and Table S13, we focus on $C_{10}H_{12}$ as an example. As can be seen, the lengths of the double bonds in cross-conjugated $C_{10}H_{12}$ are even shorter than those in linear $C_{10}H_{12}$. But the lengths of the single bonds in linear $C_{10}H_{12}$ are shorter. This trend is common to the entire tested series (See Figure 7 in the main text). The longer C-C bonds in the cross conjugated systems indicates that the Pauli repulsion between the π-bonds is larger in the cross-conjugated systems.

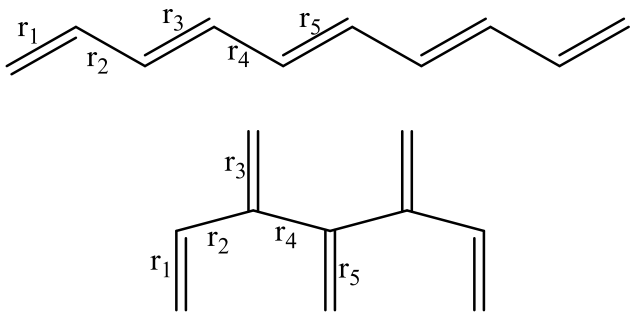

Scheme S3. Comparison of the geometries of linear and cross-conjugated $C_{10}H_{12}$.

Table S13. Geometrical parameters for linear and cross-conjugated $C_{10}H_{12}$ at B3LYP/D95V level (unit in Å).

	r_1	r_2	r_3	r_4	r_5
linear	1.359	1.456	1.370	1.447	1.372
cross	1.357	1.511	1.369	1.519	1.362

I.A.5. The geometries of the *o*-QDM and *p*-QDM molecules

Figure S1 shows the key geometric features of QDMs (Cn, n =8-20) at the B3LYP/D95V and MP2/D95V levels.

a)

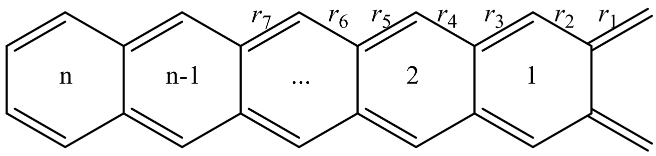

n	r_1	r_2	r_3	r_4	r_5	r_6	r_7	r_8	r_9
1	1.367	1.472	1.365						
2	1.371	1.460	1.379	1.456	1.371				
3	1.373	1.456	1.385	1.441	1.387	1.452	1.374		
4	1.374	1.453	1.388	1.436	1.394	1.436	1.391	1.450	1.375

b)

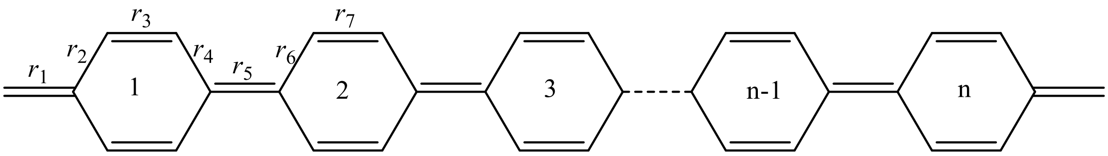

n	r_1	r_2	r_3	r_4	r_5	r_6	r_7
1	1.368	1.471	1.363				
2	1.374	1.462	1.369	1.458	1.416		
3	1.378	1.459	1.373	1.451	1.431	1.444	1.379

Figure S1. Key bond lengths (Å) for C_8-C_{20} *o*-QMD (in a), and *p*-QDM (in b) calculated at B3LYP/D95V level of theory.

II. What are the appropriate VB orbitals, HAO or BDO?

The quasiclassical state (QC) is a π-nonbonded state. Hence the difference E(QC)-E(R(0)) measures the π energy of R(0), [Eπ (R(0))].

$$E\pi(\mathrm{R}(0)) = E(\mathrm{QC}) - E(R(0)) \qquad \text{(S2.1)}$$

Eπ(full) provides the full π-energy, which includes therefore all the delocalization energy:

$$E\pi(full) = E(QC) - E(full) \qquad \text{(S2.1)}$$

The following figures S2 to S5 show the results of Eπ[R(0)] and Eπ(full) at VBSCF(HAO) and VBSCF(BDO) levels with both STO-6G and D95V.

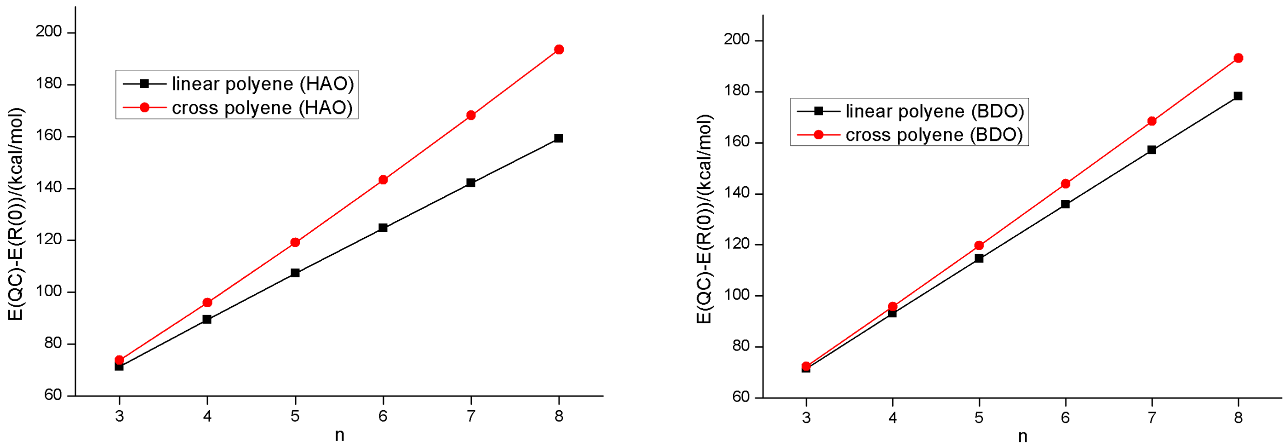

(a) (b)

Figure S2. The energy difference between $R(0)$ and the QC state at VBSCF/STO-6G level: (a) HAO, (b) BDO.

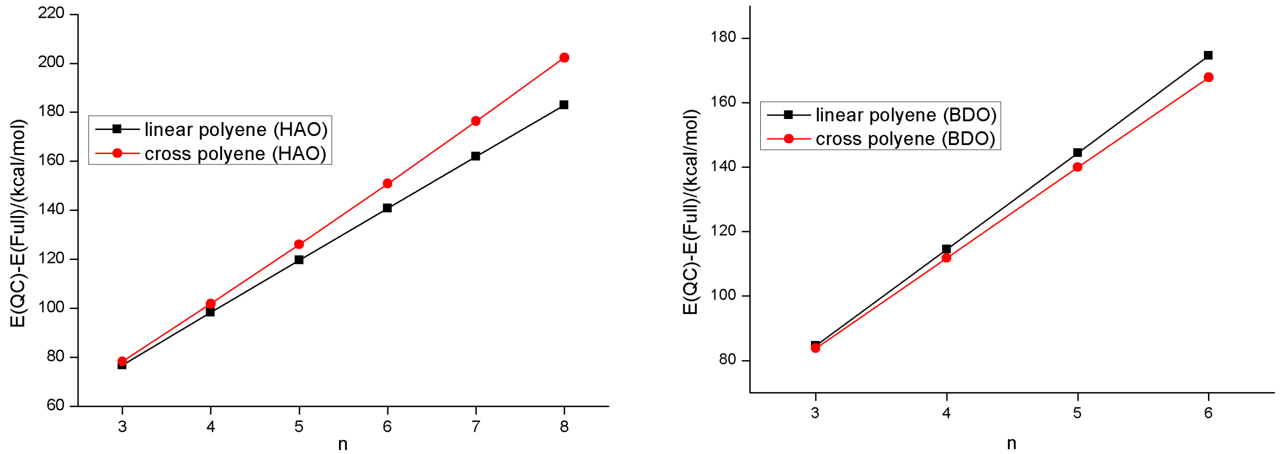

(a) (b)

Figure S3. The energy difference between Full Rumer structures and the QC state at VBSCF/STO-6G level: (a) HAO, (b) BDO.

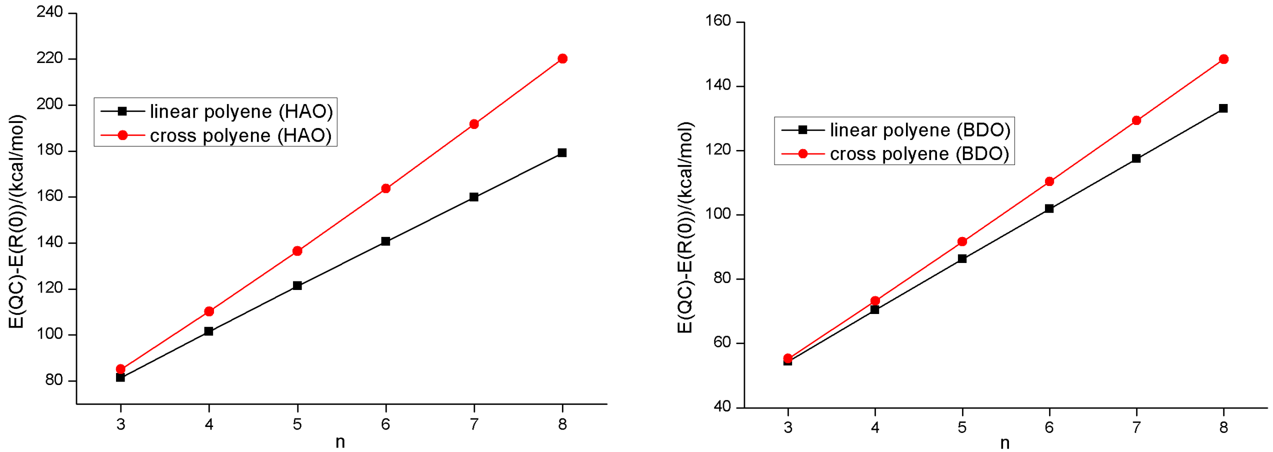

(a) (b)

Figure S4. The energy difference between $R(0)$ and the QC state at VBSCF/D95V level: (a) HAO, (b) BDO.

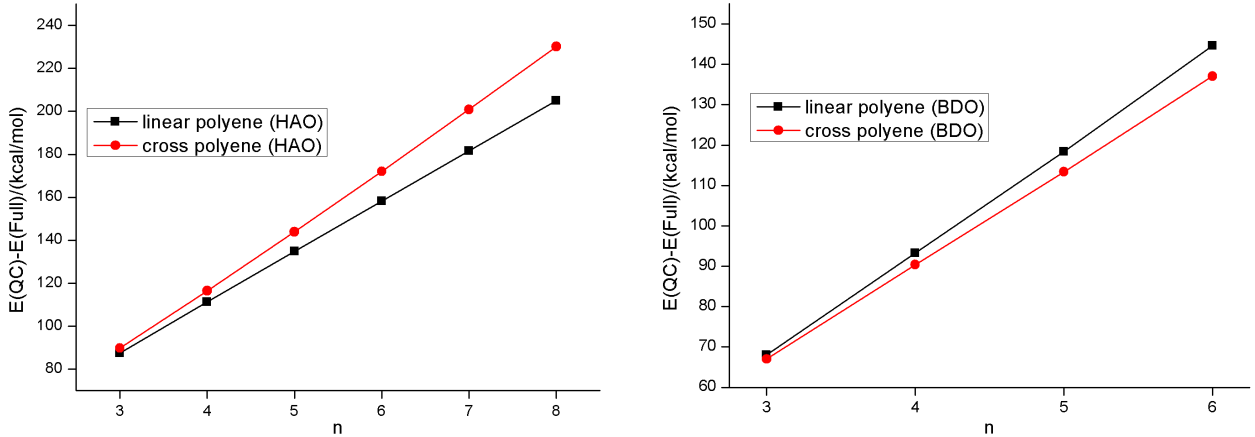

(a) (b)

Figure S5. The energy difference between Full Rumer structures and the QC state at VBSCF/D95V level: (a) HAO, (b) BDO.

From these Figures, the following conclusions can be drawn:

The cross-conjugated species has consistently larger π energy, [$E\pi$ ($R(0)$)], compared to the linear isomer. This could be due to (a) the shorter C=C bond for the cross conjugated polyenes and (b) the longer C-C which minimizes the Pauli repulsion between C=C units. So, R(0, cross) is more stabilized than R(0, linear).

On the other hand, the total π-energy [$E\pi$ (full)] is consistently larger for the linear polyenes. This is in line with the conclusion that the delocalization energy of linear polyenes is higher than that of the cross-conjugated ones.

Furthermore, Figures S2-S5, show that using HAOs exaggerates the [$E\pi$ ($R(0)$)] for the cross-conjugated species, and invert the order of [$E\pi$ (full)] values. On the other hand, with BDOs, the results are consistent; the [$E\pi$ ($R(0)$)] is higher for the cross-conjugated species, while [$E\pi$ (full)] is higher for the linear polyenes. <u>Thus, BDO emerges as the correct AO level for the problem. Both D95V and STO-6G give the same trends.</u>

Given the results presented above, we decided to optimize the geometries of cross-conjugated dendralenes at B3LYP/D95V level and do VB calculations on them at VBSCF(BDO) level with both STO-6G and D95V basis sets.

III. How to generate Rumer structures for cross-conjugated dendralenes?

1. For a given cross-conjugated molecule, move the upper carbon atom(s) down to create a cyclic system as an auxiliary molecule. For instance, for cross-conjugated C_6H_8 and C_8H_{10}, their corresponding auxiliary molecules are benzene and benzocyclobutadiene respectively.

2. Create Rumer structures for the auxiliary molecule by the Rumer rule.

For benzene, there are total five Rumer structures, two Kekulé and three Dewar structures as shown in Table S14.

3. Draw Rumer structures for the given cross-conjugated molecule by mapping the connectivity of auxiliary molecule to the cross-conjugated one. Thus, one can get a set of linearly independent Rumer structures for cross-conjugated polyene.

Tables S14-S17 show the covalent Rumer structures for cross-conjugated polyenes C_6H_8 and C_8H_{10}, linear C_8H_{10} polyenes, and C_8H_8 *o*- and *p*-QDMs. The Appendix at the end of this SI discusses a few more features of the Rumer structures and their blocks.

Table S14. Rumer structures for C_6H_8.

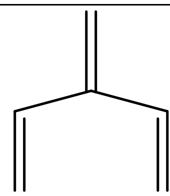	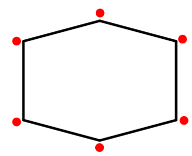
R(0)	
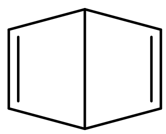	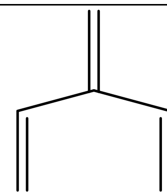
R(1)	
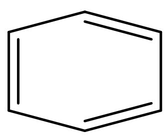	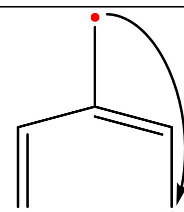
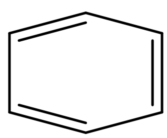	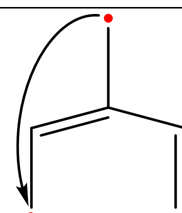
R(2)	
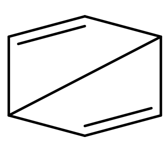	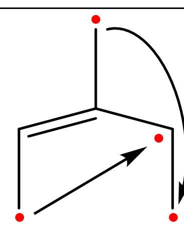
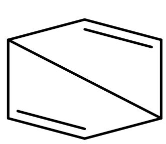	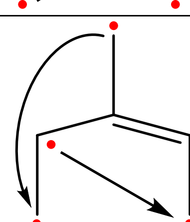

Table S15. Rumer structures for C_8H_{10}.

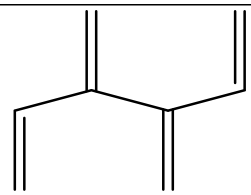	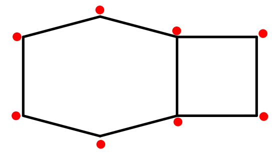
R(0)	
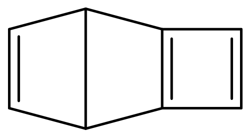	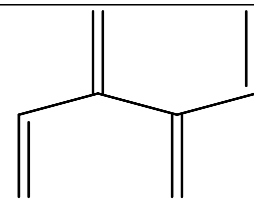
R(1)	
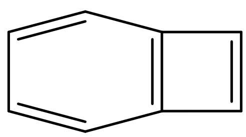	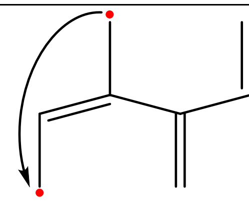
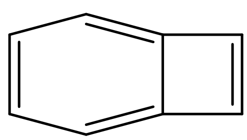	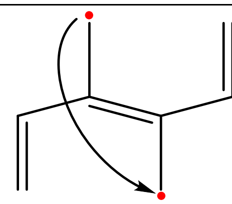
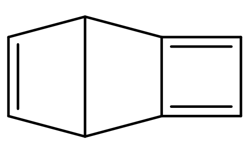	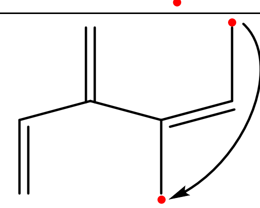
R(2)	
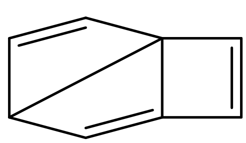	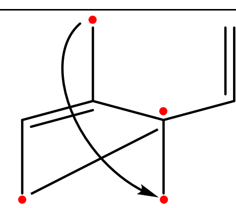
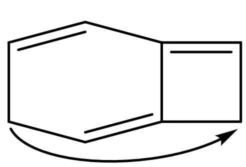	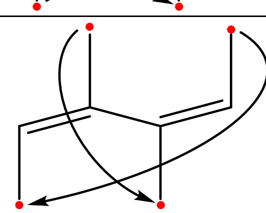

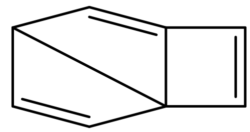	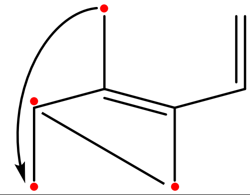
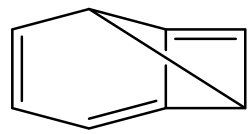	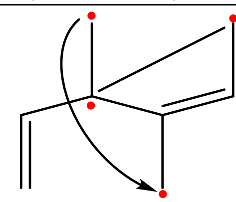
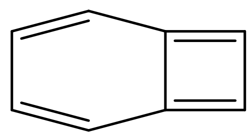	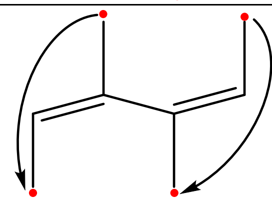
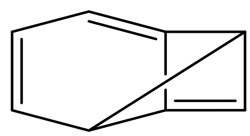	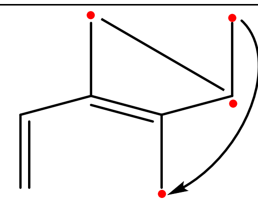
R(3)	
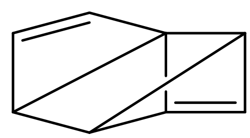	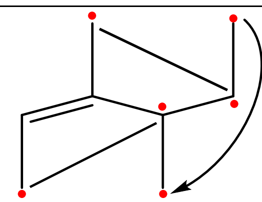
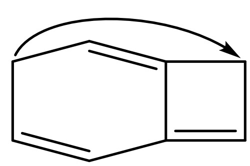	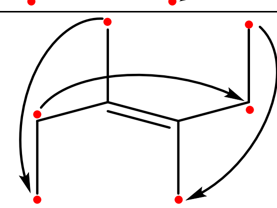
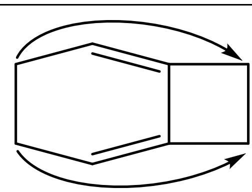	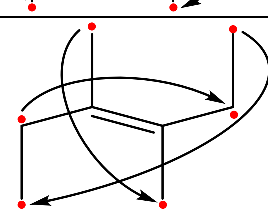
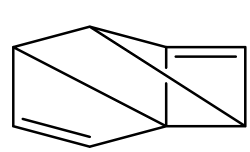	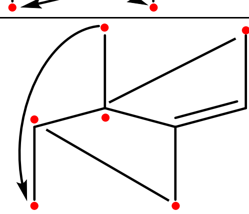

Table S16. Spectrum of the Rumer structure-set for linear polyenes C_8H_{10}.

R(0)	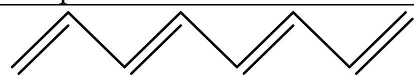
R(1)	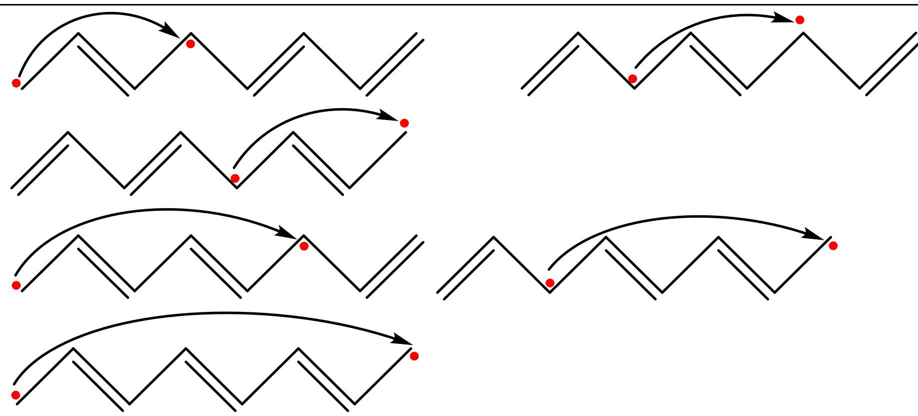
R(2)	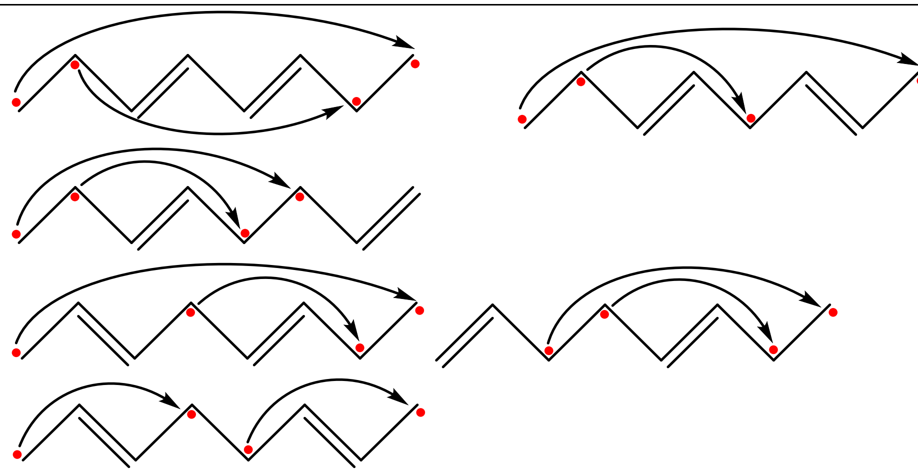
R(3)	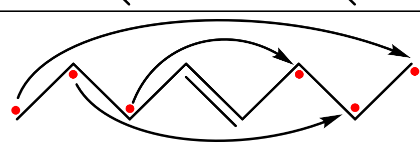

Table S17. The covalent Rumer structures for *o*- and *p*-QDM C_8H_8.

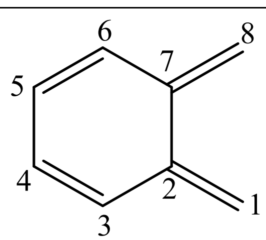	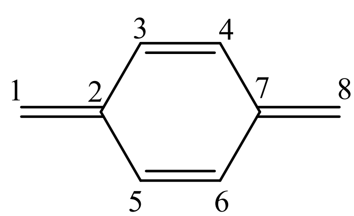
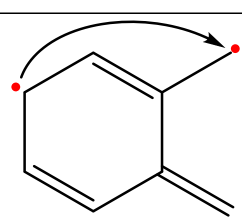	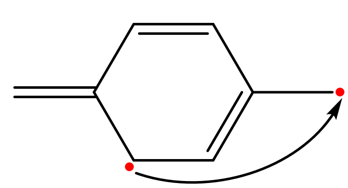

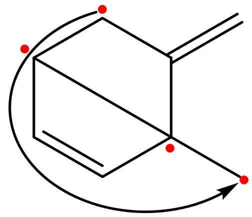	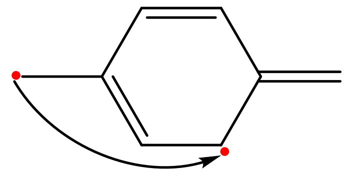
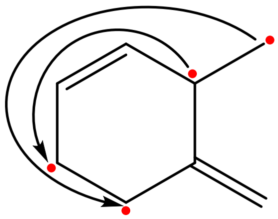	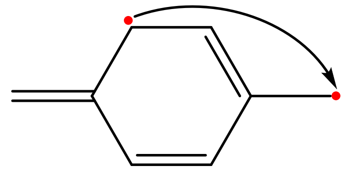
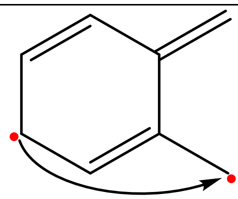	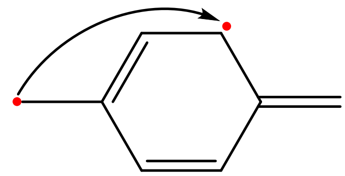
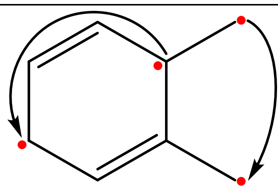	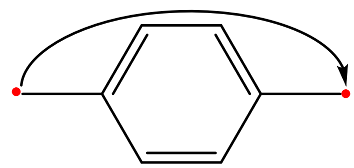
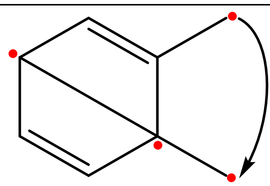	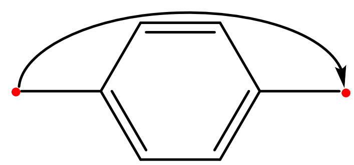
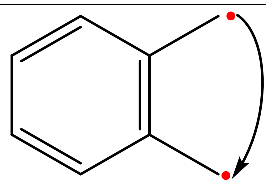	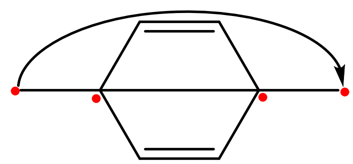
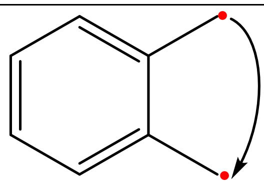	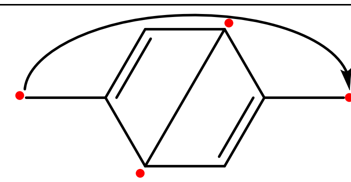
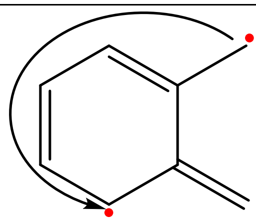	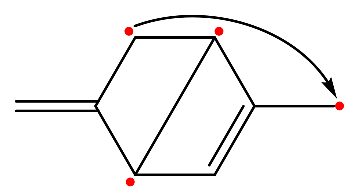

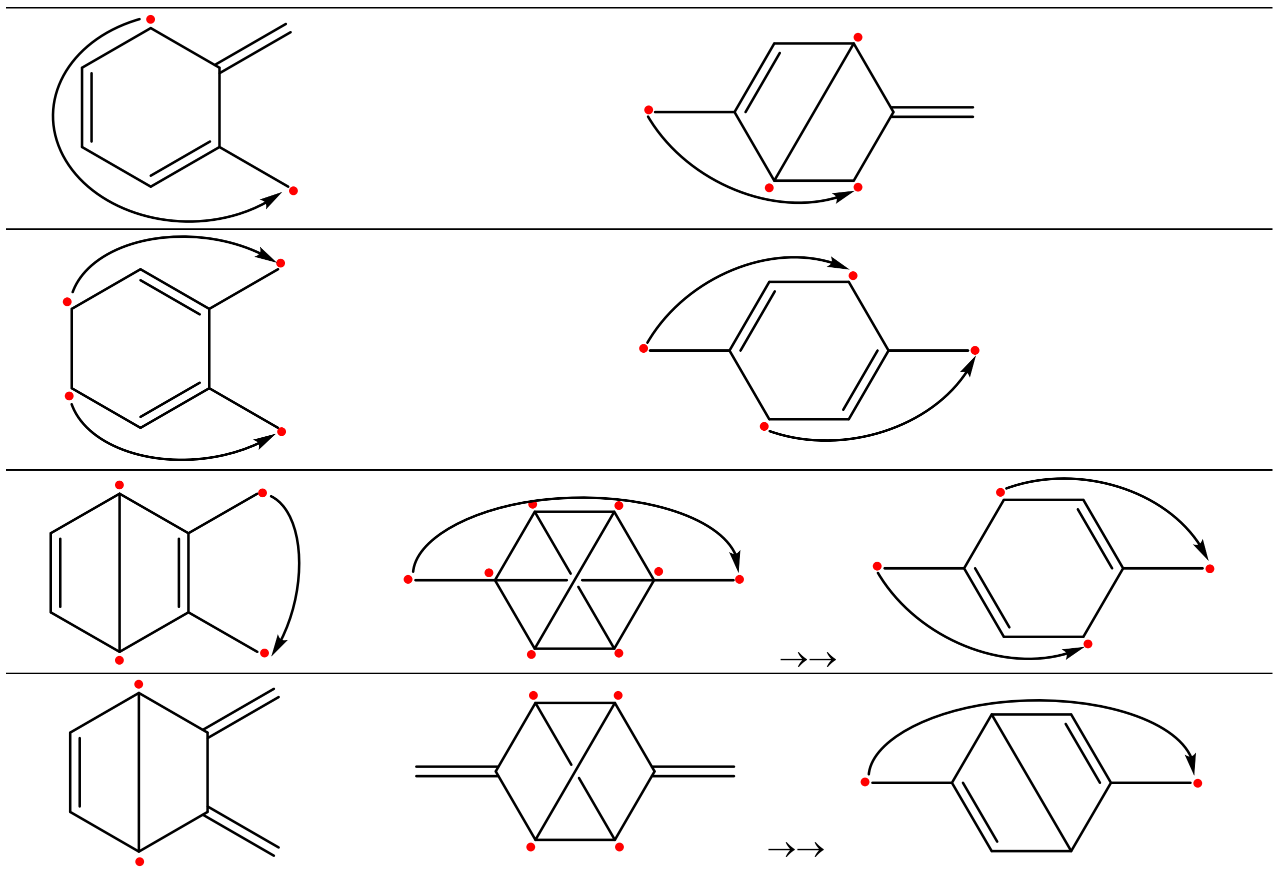

IV. $\Delta E_{HOMO\text{-}LUMO}$ and ΔE_{ST} of linear and cross-conjugated polyenes

Table S18. The HOMO-LUMO energy gap ΔE(unit in kcal mol^{-1}) for linear and cross-conjugated polyenes at B3LYP/D95V level.

Molecule	Δ*E*(linear)	Δ*E*(cross)
C_6H_8	100.5	112.7
C_8H_{10}	85.2	108.8
$C_{10}H_{12}$	74.8	107.8
$C_{12}H_{14}$	67.2	107.8
$C_{14}H_{16}$	61.4	107.4
$C_{16}H_{18}$	56.9	107.7

Table S19. The energy gap (ΔE_{ST}, in kcal mol^{-1}) of the singlet and triplet states of linear and cross-conjugated polyenes at B3LYP/D95V level.

Molecule	ΔE_{ST}(linear)	ΔE_{ST}(cross)
C_6H_8	43.3	52.4
C_8H_{10}	34.8	53.2
$C_{10}H_{12}$	29.0	54.7
$C_{12}H_{14}$	24.8	56.6
$C_{14}H_{16}$	21.6	57.4
$C_{16}H_{18}$	19.1	58.9

V. Delocalization energies in the linear and cross-conjugated polyenes

Tables S20 and S21 collect the ΔE_{del} values, respectively for the CASSCF and VBSCF(BDO-C; $R(0) + R(1,j)$) wave functions. For the sake of convenience, our definition of ΔE_{del}, in eq. 4-6 in the main text, leads to positive quantities. It is seen that the basis set makes a rather small difference, with slightly higher values for D95V.

Table S20. Delocalization energies ($\Delta E_{del\text{-}CASSCF}$[a], in kcal mol^{-1}) for linear and cross-conjugated polyenes $C_{2n}H_{2n+2}$ in the STO-6G and D95V basis sets.

Structure	ΔE_{CASSCF}(full-π) Cross-conjugated (STO-6G/D95V)	Linearly conjugated (STO-6G/D95V)	$\Delta\Delta E_{del\text{-}CASSCF}$[b] (STO-6G/D95V)
C_6H_8	18.3/19.2	21.1/21.6	2.8/2.5
C_8H_{10}	25.9/27.4	33.2/33.8	7.3/6.5
$C_{10}H_{12}$	32.6/34.6	45.6/46.3	13.0/11.7
$C_{12}H_{14}$	38.5/41.0	58.3/59.0	19.8/18.0
$C_{14}H_{16}$	43.9/46.9	71.1/71.9	27.2/25.0
$C_{16}H_{18}$	49.0/52.5	84.0/84.9	35.1/32.3

[a] $\Delta E_{\mathrm{del-CASSCF}} = E\big(R(0)\big) - \mathrm{E}_{\mathrm{CASSCF}}(n,n)$

[b] $\Delta\Delta E_{del-CASSCF} = \Delta E_{\mathrm{del-CASSCF}}(linear) - \Delta E_{\mathrm{del-CASSCF}}(cross)$

Table S21. Delocalization energies ($\Delta E_{\text{del-VBSCF(BDO-C)}}$, in kcal mol^{-1}) for linear and cross-conjugated polyenes $C_{2n}H_{2n+2}$ in the STO-6G and D95V basis sets.

Structure	$\Delta E_{\text{del-VBSCF}}$(full-π) Cross-conjugated (STO-6G/D95V)	Linearly conjugated (STO-6G/D95V)	$\Delta\Delta E_{\text{del-VBSCF}}$ [b] (STO-6G/D95V)
C_6H_8	11.4/11.8 (11.2/11.2)[c]	13.1/13.7 (13.4/13.3)[c]	1.7/1.9 (2.2/2.1)[c]
C_8H_{10}	16.0/17.2 (15.3/15.2)[c]	21.3/22.9 (20.8/20.9)[c]	5.4/5.7 (5.5/5.7)[c]
$C_{10}H_{12}$	20.3/21.8 (18.6/19.0)[c]	30.0/32.2 (28.1/28.3)[c]	9.5/10.7 (9.5/9.3)[c]
$C_{12}H_{14}$	23.9/26.7 (21.5/21.8)[c]	38.7/42.8 (35.2/35.6)[c]	14.8/16.1
$C_{14}H_{16}$	(24.9/24.8)[c]	(42.0/42.5)[c]	(17.1/17.7)[c]
$C_{16}H_{18}$	(26.3/27.3)[c]	(48.4/--)[c]	(22.1/--)[c]
$C_{18}H_{20}$	(28.5/29.9)[c]	(54.5/--)[c]	(26.0/--)[c]

[a] $\Delta E_{\text{del-VBSCF(BDO-C)}} = E\big(R(0)\big) - \mathrm{E}_{\text{VBSCF},full}$

[b] $\Delta\Delta E_{\text{del-VBSCF(BDO-C)}} = \Delta E_{\text{del}}(linear) - \Delta E_{\text{del}}(cross)$

[c] values in parentheses correspond to $\Delta \mathrm{E}_{\text{del-VBSCF(BDO-C)}} = E\big(R(0)\big) - \mathrm{E}(R(0) + R(1,j))$

The comparison of the two polyene families shows that the evaluation of ΔE_{del} using CASSCF, leads to higher delocalization energies than the VBSCF(BDO-C) method. However, for either CASSCF or VBSCF(BDO-C), the $\Delta\Delta E_{\text{del}}$ values are positive for all cases, such that the linear conjugation leads to larger delocalization energy. The CASSCF values, can be correlated against n (the number of C=C bonds), leading to the following equations for STO-6G and D95V, respectively:

$$\Delta\Delta E_{\text{del,casscf}}/\text{n (kcal/mol)} = 7.9 - 10.5 \exp[-0.14\text{n}] \qquad \text{STO-6G} \qquad \text{(S3.1)}$$

$$\Delta\Delta E_{\text{del,casscf}}/\text{n (kcal/mol)} = 7.8 - 10.1 \exp[-0.13\text{n}] \qquad \text{D95V} \qquad \text{(S3.2)}$$

$$\Delta\Delta E_{\text{del,VBSCF}}/\text{n (kcal/mol)} = 5.3 - 7.7 \exp[-0.17\text{n}] \qquad \text{STO-6G} \qquad \text{(S3.3)}$$

$$\Delta\Delta E_{del,VBSCF}/n \text{ (kcal/mol)} = 6.6 - 9.1 \exp[-0.14n] \qquad \text{D95V} \qquad (S3.4)$$

VI. Delocalization in the QDM Molecules

Table S22 gives an overview of the HOMO-LUMO gaps for the different polyene systems considered at B3LYP/D95V level of theory.

Table S22. The HOMO-LUMO energy gap ΔE(kcal/mol) for linear and cross-conjugated polyenes and *o*-, *p*-quinodimethanes at B3LYP/D95V level.

Molecule	ΔE(linear)	ΔE(cross)	ΔE(*o*-QDM)	ΔE(*p*-QDM)
C_6	100.5	112.7		
C_8	85.2	108.8	73.2	83.7
C_{10}	74.8	107.8		
C_{12}	67.2	107.8	49.8	
C_{14}	61.4	107.4		49.9
C_{16}	56.9	107.7	35.9	
C_{20}				30.8

Table S23 presents the energies of the singlet and triplet states for the *o*-QDM series calculated at different levels of theory.

Table S23. The energy of singlet and triplet states of *o*-quinodimethane series C_8H_8 to $C_{16}H_{12}$ (in a.u.).

		B3LYP			MP2		
		C_8H_8	$C_{12}H_{10}$	$C_{16}H_{12}$	C_8H_8	$C_{12}H_{10}$	$C_{16}H_{12}$
D95V	singlet	-309.5611	-463.1647	-616.7706	-308.1170	-461.0361	-613.9587
	triplet	-309.5271	-463.1556	-616.7756	-308.0745	-461.0093	-613.9352
cc-pVDZ	singlet	-309.6239	-463.2606	-616.8996	-308.6106	-461.7670	-614.9275
	triplet	-309.5888	-463.2511	-616.9047	-308.5686	-461.7421	-614.9071

As can be seen from Table S23, for $C_{16}H_{12}$, the energy of triplet state is lower than that of singlet state at B3LYP/D95V and B3LYP/cc-pVDZ level. However, at MP2 level, the singlet states for all *o*-QDM molecules are the ground states.

Table S24, whether for D95V or cc-pVDZ basis sets, shows that the OSS of $C_{16}H_{12}$ has a lower energy at the UB3LYP level. However, MP2 gives a lower energy for the singlet state of $C_{16}H_{12}$. The energy gap between singlet and triplet states is less than 20 kcal/mol at either UB3LYP or UMP2 levels.

Table S24. The energy of singlet and triplet states of ortho-quinodimethane $C_{16}H_{12}$ (in a.u.).

	UB3LYP				UMP2	
	singlet	Triplet	OSS	S^2-OSS	singlet	triplet
D95V	-616.7706	-616.7756	-616.7819	1.07	-613.9587	-613.9352
cc-pVDZ	-616.8996	-616.9047	-616.9105	1.06	-614.9275	-614.9071

Table S25 summarized the VBSCF/D95V based energies for both singlet and triplet states of $C_{16}H_{12}$, whose geometries were optimized at both B3LYP/D95V and MP2/D95V levels respectively. The energies based on both HAO and OEO prefer the singlet state for the ground state of $C_{16}H_{12}$. We can find that the energy of singlet state is ~20 kcal/mol lower than that of triplet state, which suggests that ***the ground state is singlet for o-quinodimethane series C_8H_8 to $C_{16}H_{12}$.***

Table S25. Energy of the singlet and triplet states of *o*-quinodimethane $C_{16}H_{12}$ at VBSCF/D95V level based on covalent Rumer structures (in a.u.).

	B3LYP/D95V geometry		MP2/D95V geometry	
	singlet	triplet	singlet	triplet
E(HAO)	-612.4994	-612.4678	-612.5053	-612.4635
E(OEO)	-612.8573	-612.8340	-612.8497	-612.8218

So, from the data of both MO and VB theory, we can conclude the ground state of $C_{16}H_{12}$ is singlet. Nevertheless, the very low ΔE_{ST} values are indicators of increasing diradicaloid nature in the *o*-QDMs. Very similar conclusions apply to *p*-QDMs as seen from Table S26.

Table S26. The singlet-triplet energy gap (ΔE_{ST}, in kcal mol^{-1}) for *p*-quinodimethane series calculated at different levels of theory.

	B3LYP/STO-6G	B3LYP/D95V	MP2/STO-6G	MP2/D95V
C_8	27.4	30.0	31.1	32.9
C_{14}	0.6	7.6	18.6	/

C_{20}	-15.1	-7	/	/

To test the extent by which the DFT results for ΔE_{ST} are functional dependent, we replicated the DFT calculations for the longest analogues of both *o*-QDM (C_{16}) and *p*-QDM (C_{20}) with a variety of different functionals (PBEEh1PBE, CAM-B3LYP and M06-2X). The results are summarized in Table S27 below. One can conclude that the results for each of these functionals point in the same direction (i.e., the triplet state is slightly lower in energy than the singlet state).

Table S27. The singlet-triplet energy gap (ΔE_{ST}, in kcal mol^{-1}) for the longest analogues of both *o*-QDM (C_{16}) and *p*-QDM (C_{20}) calculated with different functionals with the D95V basis set.

	B3LYP	PBEEh1PBE	CAM-B3LYP	M06-2X
C_{16} o-QDM	-3.2	-5.6	-6.0	-0.4
C_{20} p-QDM	-7.0	-9.4	-17.5	-9.9

Table S28 gives an overview of the energy gaps between the lowest singlet and triplet state for the different polyene systems considered at B3LYP/D95V level of theory.

Table S28. The energy gap (ΔE, in kcal mol^{-1}) of the singlet and triplet states for the linear and cross-conjugated polyenes and the quinodimethane series at B3LYP/D95V level.

Molecule	ΔE(linear)	ΔE(cross)	ΔE(*o*-QDM)	ΔE(*p*-QDM)
C_6	43.3	52.4		
C_8	34.8	53.2	21.3	30.0
C_{10}	29.0	54.7		
C_{12}	24.8	56.6	5.7	
C_{14}	21.6	57.4		7.6
C_{16}	19.1	58.9	-3.2	
C_{20}				-7.0

VII. Comparison of the three families

The following tables give an overview of the delocalization and π-energies for the linear and cross-conjugated systems $C_{2n}H_{2n+2}$ and *o*-, *p*-quinodimethanes at VBSCF(BDO)/STO-6G and VBSCF(BDO)/D95V.

Table S29. Delocalization energies (ΔE_{del} [a], in kcal mol^{-1}) for linear and cross-conjugated systems $C_{2n}H_{2n+2}$ and *o*-, *p*-quinodimethanes at VBSCF(BDO)/STO-6G level.

Structure	$\Delta E_{\text{del-CASSCF}}$ (linear)	$\Delta E_{\text{del-CASSCF}}$ (cross)	$\Delta E_{\text{del-CASSCF}}$ (*o*-QDM)	$\Delta E_{\text{del-CASSCF}}$ (*p*-QDM)
C_6	21.12	18.30		
C_8	33.19	25.94	40.50	41.43
C_{10}	45.59	32.58		
C_{12}	58.29	38.49	79.47	
C_{14}	71.09	43.86		96.09
C_{16}	84.02	48.95	122.84	

[a] $\Delta E_{del-CASSCF} = E(R(0)) - E_{CASSCF}(n,n)$

Table S30. Delocalization energies (ΔE_{del} [a], in kcal mol^{-1}) for linear and cross-conjugated systems $C_{2n}H_{2n+2}$ and *o*-, *p*-quinodimethanes at VBSCF(BDO)/D95V level.

Structure	$\Delta E_{\text{del-CASSCF}}$ (linear)	$\Delta E_{\text{del-CASSCF}}$ (cross)	$\Delta E_{\text{del-CASSCF}}$ (*o*-QDM)	$\Delta E_{\text{del-CASSCF}}$ (*p*-QDM)
C_6	21.63	19.18		
C_8	33.81	27.35	41.06	42.32
C_{10}	46.29	34.56		
C_{12}	59.04	41.02	79.77	
C_{14}	71.89	46.92		96.06
C_{16}	84.85	52.53	122.65	

Table S31. The Eπ[a] (unit in kcal mol^{-1}) for linear and cross-conjugated $C_{2n}H_{2n+2}$ and *ortho*-, *para*-quinodimethanes at VBSCF/STO-6G level.

Structure	*E*π(linear)	*E*π(cross)	*E*π(*o*-QDM)	*E*π(*p*-QDM)
C_6	71.5	72.4		
C_8	93.1	95.8	89.6	89.7
C_{10}	114.6	119.7		
C_{12}	135.9	143.9	126.2	
C_{14}	157.1	168.5		145.9
C_{16}	178.2	193.1	161.0	

[a] *E*π = *E*(QC)-*E*(*R*(0))

Table S32. The Eπ (unit in kcal mol^{-1}) for linear and cross-conjugated $C_{2n}H_{2n+2}$ and *o*-, *p*-quinodimethanes at VBSCF(BDO)/D95V level.

Structure	Eπ(linear)	Eπ(cross)	Eπ(*o*-QDM)	Eπ(*p*-QDM)
C_6	54.4	55.3		
C_8	70.4	73.2	66.6	67.6
C_{10}	86.2	91.6		
C_{12}	101.9	110.4	90.8	
C_{14}	117.5	129.3		106.6
C_{16}	133.0	148.4	112.9	

VIII. VB perturbation energy for calculating the delocalization energy using *R*(0) as the reference state

$$\beta_i = H_{0,i} - H_{0,0}S_{0,i} \tag{S8.1}$$

where 0 and *i* are the Rumer structure in group *R*(0) and the other groups respectively.

$$\Delta E_{del-Pert} = \sum_i (\Delta E_{0,i}) = \sum_i |C_i \beta_i| \tag{S8.2}$$

$$\Delta E_{del-VBSCF} = E\big(R(0)\big) - E(full) \tag{S8.3}$$

Table 8 in the main text shows that the perturbation energy expression predicts quite well the delocalization energy of the two polyene types. Furthermore, we find that the delocalization energy for the linear polyenes is consistently larger than the same property for the cross conjugation.

In Table S33 and Figure S6, we show the delocalization energies obtained from only the first and second Rumer block.

Table S33. The delocalization energies ($\Delta E_{\text{del-VBSCF}}$ and $\Delta E_{\text{del-VBSCF}}/n$; unit in kcal mol^{-1}) for *cross-conjugated* polyenes as a function of the size *n*.[a]

	STO-6G		D95V	
	$\Delta E_{\text{del-VBSCF}}$	$\Delta E_{\text{del-VBSCF}}/n$	$\Delta E_{\text{del-VBSCF}}$	$\Delta E_{\text{del-VBSCF}}/n$
C_6H_8	11.2	3.7	11.2	3.8
C_8H_{10}	15.3	3.8	15.2	3.8
$C_{10}H_{12}$	18.6	3.7	19.0	3.8
$C_{12}H_{14}$	21.5	3.6	21.8	3.6
$C_{14}H_{16}$	24.0	3.4	24.8	3.5
$C_{16}H_{18}$	26.3	3.3	27.3	3.4
$C_{18}H_{20}$	28.5	3.2	29.9	3.3

[a] $\Delta E_{\text{del-vbscf(BDO-C)}} = (E(R(0)) - E(R(0) + R(1,j)))$

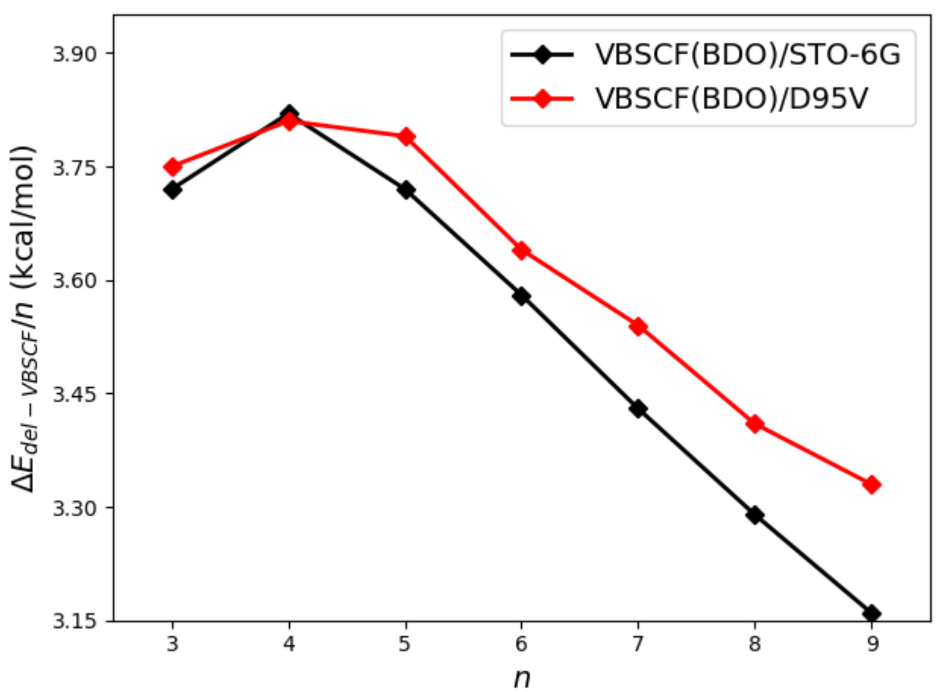

Figure S6. The trends for $\Delta E_{\text{del-vbscf}}/n$ as n gets larger for the cross-conjugated polyenes at

VBSCF(BDO) level when only *R*(0) and *R*(1) are taken into account.

In table S34, the corresponding $\Delta E_{\text{del-VBSCF}}[C_n\text{-}C_{n-1}]$ are presented.

Table S34. The delocalization energies (unit in kcal mol^{-1}) for *cross-conjugated* polyenes at VBSCF(BDO) level.[a,b]

	STO-6G		D95V	
	$\Delta E_{\text{del-VBSCF}}$	$\Delta E_{\text{del-VBSCF}}[C_n\text{-}C_{n-1}]$[a]	$\Delta E_{\text{del-VBSCF}}$	$\Delta E_{\text{del-VBSCF}}[C_n\text{-}C_{n-1}]$[a]
C_6H_8	11.2	---	11.2	---
C_8H_{10}	15.3	4.1	15.2	4.0
$C_{10}H_{12}$	18.6	3.4	19.0	3.7
$C_{12}H_{14}$	21.5	2.9	21.8	2.9
$C_{14}H_{16}$	24.0	2.5	24.8	3.0
$C_{16}H_{18}$	26.3	2.3	27.3	2.5
$C_{18}H_{20}$	28.5	2.2	29.9	2.7

[a] $\Delta E_{\text{del-VBSCF(BDO-C)}} = \left(E\left(R(0)\right) - E\left(R(0) + R(1,j)\right)\right)$

[b] $\Delta E_{\text{del-VBSCF}}[C_n\text{-}C_{n-1}] = \Delta E_{\text{del-VBSCF}}(C_n) - \Delta E_{\text{del-VBSCF}}(C_{n-1})$

IX. Comparison of the perturbation energy contributions in the three families

Table S35. The individual terms for the predicted delocalization energies for both *p*-QDM C_8H_8 at VBSCF(BDO) level.

	STO-6G			D95V		
	C_i	β_i	$\Delta E_{0,i}$ (kcal/mol)	C_i	β_i	$\Delta E_{0,i}$ (kcal/mol)
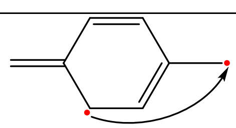	-0.153	0.0528	-5.08	-0.152	0.0537	-5.12
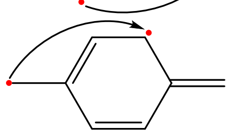	-0.153	0.0528	-5.08	-0.151	0.0538	-5.09
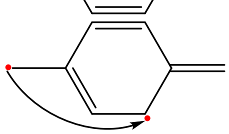	-0.135	0.0538	-4.57	-0.135	0.0550	-4.65

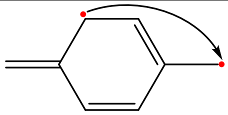	-0.135	0.0538	-4.57	-0.132	0.0553	-4.57
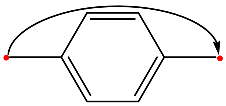	0.070	-0.0427	-1.86	0.060	-0.0405	-1.52
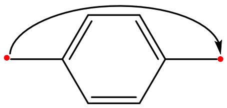	0.070	-0.0427	-1.86	0.061	-0.0405	-1.56

Table S36. The individual terms for the predicted delocalization energies for both *o*-QDM C_8H_8 at VBSCF(BDO) level.

	STO-6G			D95V		
	C_i	β_i	$\Delta E_{0,i}$ (kcal/mol)	C_i	β_i	$\Delta E_{0,i}$ (kcal/mol)
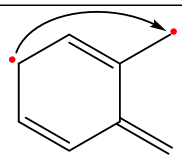	-0.172	0.0535	-5.76	-0.178	0.0529	-5.92
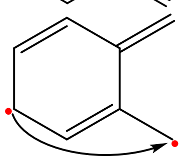	-0.172	0.0535	-5.76	-0.150	0.0537	-5.06
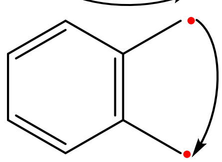	-0.160	0.0497	-5.00	-0.171	0.0502	-5.39
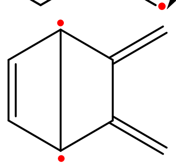	-0.183	0.0544	-6.24	-0.151	0.0558	-5.28
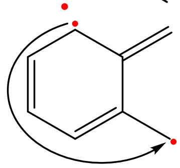	-0.014	-0.0027	0.02	0.032	-0.0358	-0.71
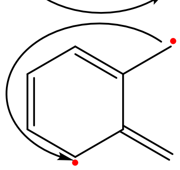	-0.014	-0.0027	0.02	0.026	-0.0351	-0.57
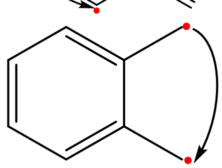	-0.103	0.0320	-2.06	-0.081	0.0366	-1.86

Table S37. The individual terms for the predicted delocalization energies for both cross-conjugated C_8H_{10} at VBSCF(BDO) level.

	STO-6G			D95V		
	C_i	β_i	$\Delta E_{0,i}$ (kcal/mol)	C_i	β_i	$\Delta E_{0,i}$ (kcal/mol)
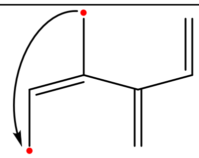	-0.165	0.0501	-5.18	-0.162	0.0503	-5.10
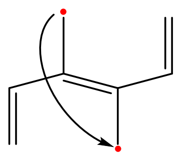	-0.173	0.0494	-5.34	-0.158	0.0495	-4.91
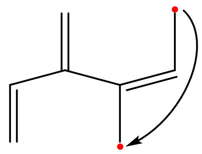	-0.165	0.0501	-5.18	-0.153	0.0508	-4.87

Table S38. The individual terms for the predicted delocalization energies for both linear C_8H_{10} at VBSCF(BDO) level.

	STO-6G			D95V		
	C_i	β_i	$\Delta E_{0,i}$ (kcal/mol)	C_i	β_i	$\Delta E_{0,i}$ (kcal/mol)
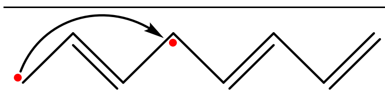	-0.166	0.0542	-5.65	-0.158	0.0546	-5.43
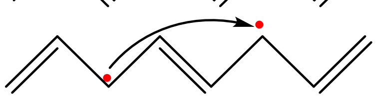	-0.157	0.0553	-5.46	-0.158	0.0571	-5.67
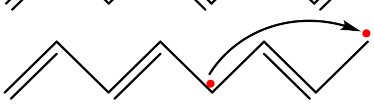	-0.166	0.0542	-5.65	-0.159	0.0546	-5.44
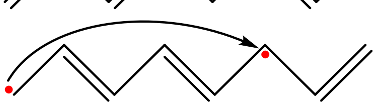	0.057	-0.0436	-1.55	0.052	-0.0415	-1.36
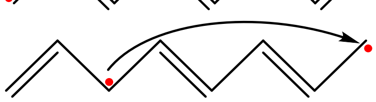	0.057	-0.0436	-1.55	0.052	-0.0417	-1.36
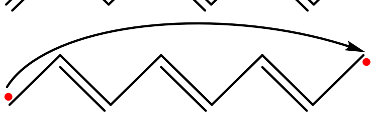	-0.048	0.0262	-0.78	-0.046	0.0299	-0.87

X. Decay-rate in the weight of the fundamental structure, W(R(0))

The W(R(0)) values decrease with the length of the polyene. The decrease is tempered for the cross polyenes, as expected from the lesser mixing of $R(1)$ Rumers into $R(0)$.

Table S39. Comparison of the computed and predicted weight W(R(0)) of the Cross-conjugated $C_{2n}H_{2n+2}$ at VBSCF(BDO)/D95V level.

	W(R(0))	W(R(0))[a]
C_4H_6[b]	0.871	0.871
C_6H_8	0.777	0.813
C_8H_{10}	0.704	0.759
$C_{10}H_{12}$	0.637	0.708
$C_{12}H_{14}$	0.596	0.661

[a] based on eq. a.
[b] $W_2(0)=3^{1/2}/2$, which is very close to 0.877.

Table S40. The number of Rumer structures in each blocks for cross-conjugated $C_{2n}H_{2n+2}$.

$C_{2n}H_{2n+2}$	***R*(0)**	***R*(1)**	***R*(2)**	***R*(n-1)**
C_6H_8	1	2	2	
C_8H_{10}	1	3	6	4
$C_{10}H_{12}$	1	4	11	8
$C_{12}H_{14}$	1	5	17	16
$C_{14}H_{16}$	1	6	24	32
$C_{16}H_{18}$	1	7	32	64
$C_{18}H_{20}$	1	8	41	128

Table S41. The number of Rumer structures in each blocks for linear $C_{2n}H_{2n+2}$.

$C_{2n}H_{2n+2}$	***R*(0)**	***R*(1)**	***R*(2)**	***R*(n-1)**
C_6H_8	1	3	1	
C_8H_{10}	1	6	6	1
$C_{10}H_{12}$	1	10	20	1
$C_{12}H_{14}$	1	15	50	1
$C_{14}H_{16}$	1	21	105	1
$C_{16}H_{18}$	1	28	196	1
$C_{18}H_{20}$	1	36	336	1

XI. APPENDIX 1: Does *s*-cis butadiene have a skewed [gauche] conformation?

To comprehend the skewing driving force in dendralenes, we optimized the geometry of skew C_4H_6 at B3LYP/D95V level as shown in the drawing below, in which the dihedral (C3,C1,C5,C7)-angle is 24°.

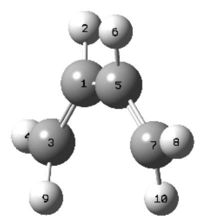

Figure A1.1. The geometry for the skew C_4H_6.

We found that *cis* conformer of C_4H_6 has an imaginary frequency of 103i cm^{-1}, while the skewed one has no imaginary frequency. So, the skewed conformer of C_4H_6 is a real minimum, but the *cis* one is not.

From the table below, we can see that the skewed conformer is only 0.1 kcal/mol lower than the *cis* one and about 2 kcal/mol higher than the *trans* one.

Table A1.1. The energy (unit in a.u.) for *cis*, skew and *trans* C_4H_6 at VBSCF/D95V level with both HAO and BDO.

	E(*cis*-C_4H_6)	*E*(skew C_4H_6)	*E*(*trans*-C_4H_6)
HAO	-154.8615	-154.8616	-154.8648
BDO	-154.9261	-154.9263	-154.9304

Table A1.2. Comparison of the weight W(R(0)) between *cis*, skew and *trans* C_4H_6 at VBSCF/D95V level with both HAO and BDO.

	cis-C_4H_6	skew C_4H_6	*trans*-C_4H_6
W(R(0),HAO)	0.887	0.907	0.877
W(R(0),BDO)	0.883	0.897	0.871

As can be seen from the above weights of *R*(0), the value W(*R*(0)) for the skewed C_4H_6 is larger than that of both cis and trans ones, which indicate that the skew one is more localized. This is the same as concluded above for the smallest cross-conjugated polyene. Furthermore, in butadiene we found in a previous paper[3] that $R(0)$ determines the rotational barrier of the trans butadiene. This is similar to our findings for the [3]dendralene, which are re-copied here below, that $R(0)$ determines the preference for skewing the geometry in the dendralene.

Table A1.3. The energy (unit in a.u.) of $R(0)$ of cross-conjugated C_6H_8 at VBSCF/D95V level.

	E(R(0),HAO)	E(R(0),BDO)
planar C_6H_8	-231.6981	-231.7898
skew C_6H_8	-231.7038	-231.7950

XII. APPENDIX 2: VB expansion of the VBSCF(BDO-C) for butadiene

Butadiene has two Rumer structures $R(0)$ and $R(1)$ (Fig. A2.1)

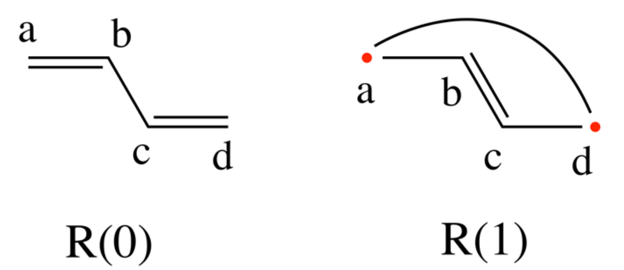

Figure A2.1. The VBSCF(BDO-C) wave function for butadiene.

Using BDOs, the p_π AOs have tails on the bonded atoms:

For $R(0)$,

$$p_a = \langle a| + \lambda \langle b| , \qquad p_b = \langle b| + \lambda \langle a|$$
$$p_c = \langle c| + \lambda \langle d| , \qquad p_d = \langle d| + \lambda \langle c| \tag{A2.1}$$

For $R(1)$,

$$p_a = \langle a| + \lambda \langle d| , \qquad p_d = \langle d| + \lambda \langle a| \tag{A2.2}$$

$$p_b = \langle b| + \lambda \langle c| , \qquad p_c = \langle c| + \lambda \langle b|$$

Writing $R(0)$ and $R(1)$ as Slater determinants, while droping the normalization constants and the anti-symmetrizer operator symbol, we get:

$$R(0) = \left|\left[\left(p_a(1)\overline{p_b}(2)\right) - \left(\overline{p_a}(1)p_b(2)\right)\right]\right| * \left|\left[\left(p_c(3)\overline{p_d}(4)\right) - \left(\overline{p_c}(3)p_d(4)\right)\right]\right| \quad \text{(A2.3)}$$

$$R(1) = \left|\left[\left(p_a(1)\overline{p_d}(2)\right) - \left(\overline{p_a}(1)p_d(2)\right)\right]\right| * \left|\left[\left(p_b(3)\overline{p_c}(4)\right) - \left(\overline{p_b}(3)p_c(4)\right)\right]\right| \quad \text{(A2.4)}$$

Here, the Slater determinants are expressed in terms of the respective diagonal terms. 1-4 are the electron numbers, which are dropped in what follows.

If we substitute the expression of the BDO (p_a – p_d) by their HAO expression in eqs. A2.3 and A2.4, and expand the determinants, we get the following terms,

$$R(0) \sim (1+\lambda^2)^2\left|\left(a\bar{b} - \bar{a}b\right)\left(c\bar{d} - \bar{c}d\right)\right| + 2\lambda(1+\lambda^2)\left\{\left|\left(a\bar{b} - \bar{a}b\right)\left(c\bar{c} - \bar{d}d\right)\right| + \left|\left(a\bar{a} - \bar{b}b\right)\left(c\bar{d} - \bar{c}d\right)\right|\right\} + 4\lambda^4\left\{\left|\left(a\bar{a}c\bar{c}\right)\right| + \left|\left(a\bar{a}d\bar{d}\right)\right| + \left|\left(b\bar{b}c\bar{c}\right)\right| + \left|\left(b\bar{b}d\bar{d}\right)\right|\right\} \quad \text{(A2.5)}$$

Pictorially, we express $R(0)$ as follows (Fig. A2.2).

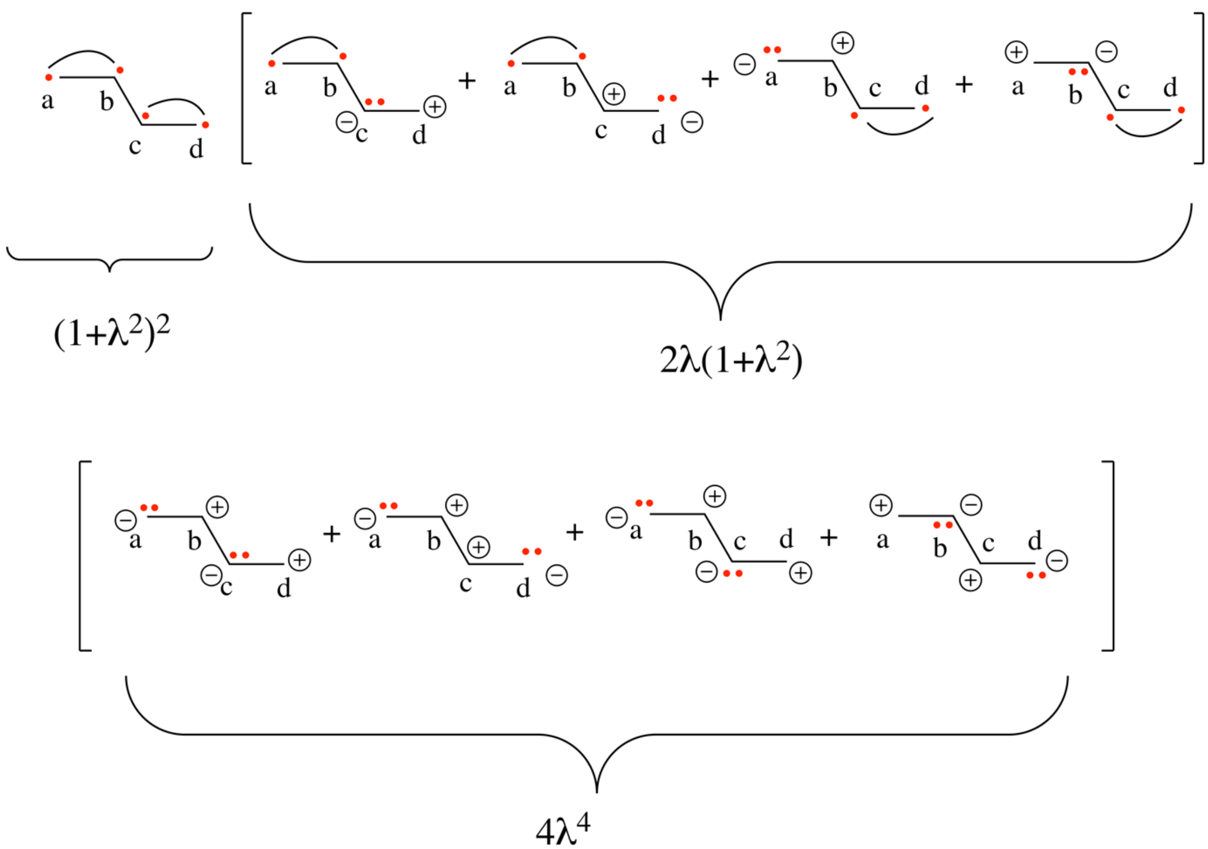

Figure A2.2. Pictorial representation of the HAO expansion of $R(0)$ in the VBSCF(BDO-C) wave function for butadiene.

It is seen that with the BDOs, $R(0)$ involves the purely covalent $R(0)$, four mono-ionic structures, and four diionic structures.

Similarly, expanding $R(1)$ after substituting the BDO expressions for $p_a - p_d$ (assuming the same tails λ as in R(0)), we get the following HAO-based VB structures for $R(1)$ (Fig. A2.3).

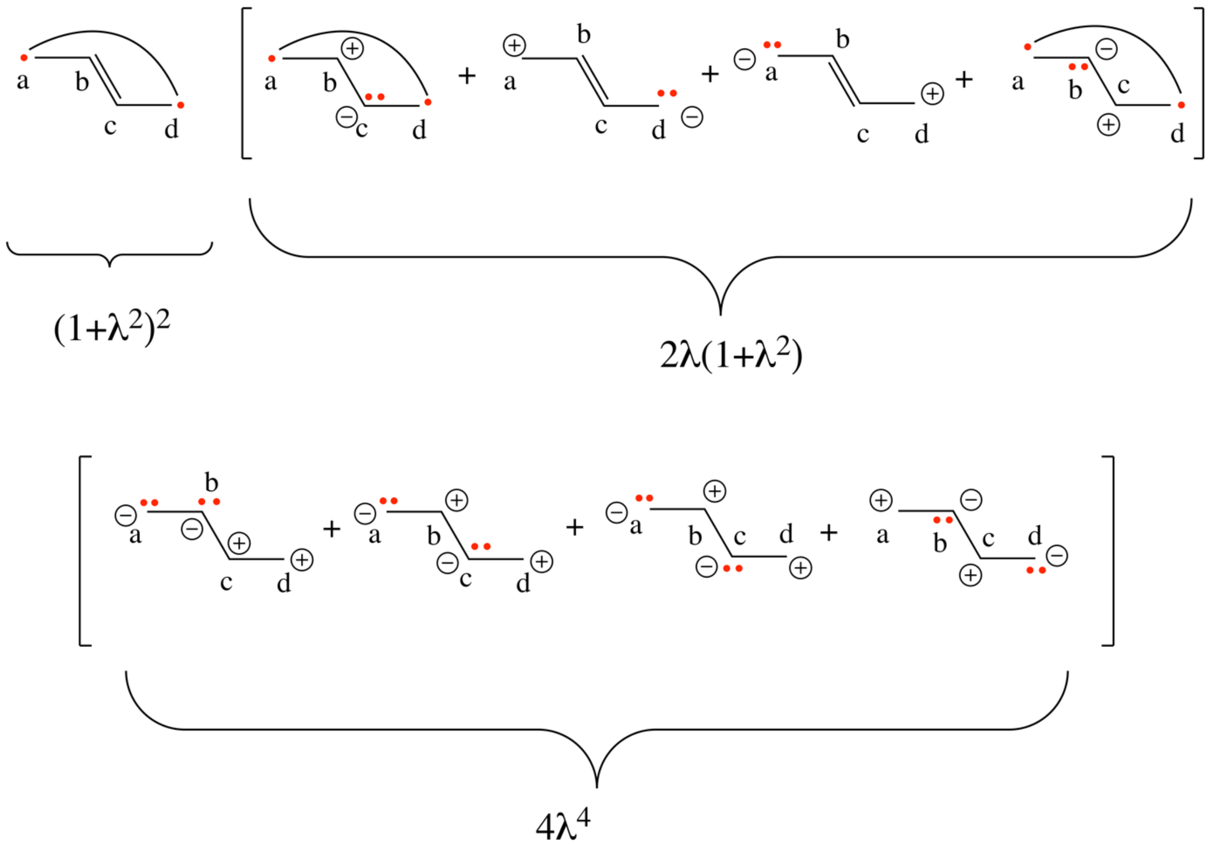

Figure SA2.3. Pictoral representation of the HAO expansion of R(1) in the VBSCF(BDO-C) wave function for butadiene.

Again, $R(1)$ involves the covalent $R(1)$ with a long bond between the (a) and (d) HAOs, four mono-ionic structures and four diionic ones.

The BDO wave function is given as:

$$\Psi(BDO, butadiene) \sim R_{BDO}(0) - cR_{BDO}(1) \qquad \text{(A2.6)}$$

where c is the coefficient. As such, butadiene is described by a purely covalent part:

$$\Psi_{HAO} = (1+\lambda^2)^2[R_{HAO}(0) - cR_{HAO}(1)] \qquad \text{(A2.7)}$$

And smaller weights of ionic structures

$$\Psi_{Mono-ionic} = (2\lambda(1+\lambda^2) - c)\Phi_{Mono-ionic} \tag{A2.8}$$

$$\Psi_{Diionic} = (4\lambda^4 - c)\Phi_{Diionic} \tag{A2.9}$$

XIII. APPENDIX 3: Rumer structures in different blocks

a) Linear and cross-conjugated polyenes

For linear $C_{2n}H_{2n+2}$, the equations for the number of Rumer structures in different blocks are shown below

$$d_1 = \binom{n}{2} \tag{A3.1}$$

$$d_2 = 2\binom{n}{4} + \binom{n}{3} \tag{A3.2}$$

$$d_{n-1} = 1 \tag{A3.3}$$

While for cross-conjugated $C_{2n}H_{2n+2}$, the numbers of Rumer structures in different blocks are shown below.

$$d_1 = n - 1 \tag{A3.4}$$

Explanation: Only each adjacent pair of double bonds in *R*(0), which can be taken as a 1,3-butadiene unit, can form a *R*(1), so d_1 equals to the number of single bonds or the unit of 1,3-butadiene in *R*(0).

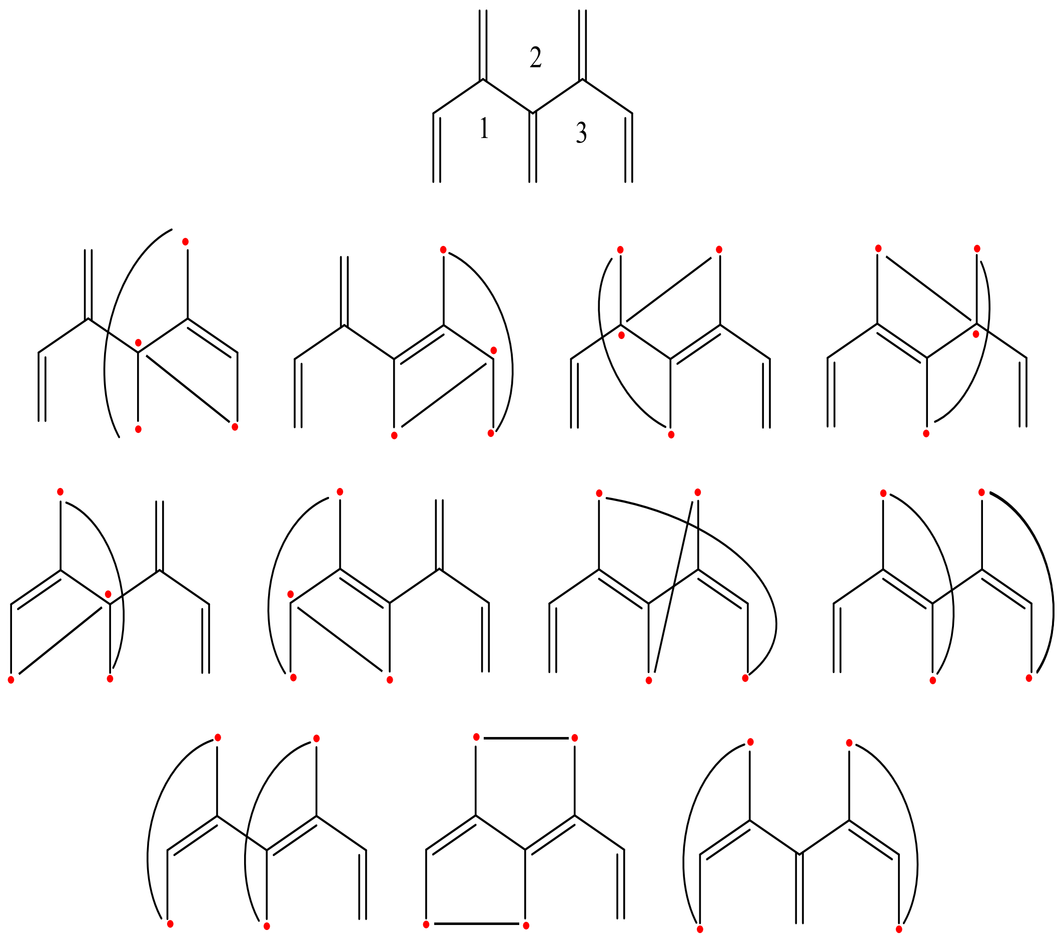

Scheme A3.1. The 3 C_6H_8 units of $C_{10}H_{12}$ and its 11 Rumer structures in R(2) block.

$$d_2 = \frac{1}{2}(n^2 + n - 8) \tag{A3.5}$$

Explanation: From the structures of $C_{10}H_{12}$ in *R*(2) block, we can find that every C_6H_8 unit can create 2 Rumer structures in *R*(2) block and every two adjacent C_6H_8 units (they have one 1,3-butadiene in common) also can create 2 Rumer structures in *R*(2) block, but every two non-adjacent C_6H_8 units only can create 1 Rumer structures in *R*(2) block.

For $C_{10}H_{12}$ in Scheme A3.1, there are 3 C_6H_8 units, which leads to 2*3=6 Rumer structures in *R*(2) block. In addition, there are 2 pairs of adjacent C_6H_8 units, i.e. 1-2, 2-3, and they will result in 2*2=4 Rumer structures in *R*(2) block. Finally, there is 1 pair of non-adjacent C_6H_8 units 1-3, which gives 1 Rumer structures. So there are 6+4+1=11 Rumer structures in *R*(2) block in total.

For general cross-conjugated $C_{2n}H_{2n+2}$, there are (n-2) C_6H_8 units and (n-3) adjacent C_6H_8 units. There are also non-adjacent C_6H_8 units, the number of which is shown below

$$[\binom{2}{n-2}-(n-3)] \tag{A3.6}$$

So we can get the following equation:

$$d_2 = 2*(n-2)+2*(n-3)+[\binom{2}{n-2}-(n-3)] = \frac{1}{2}(n^2+n-8) \tag{A3.7}$$

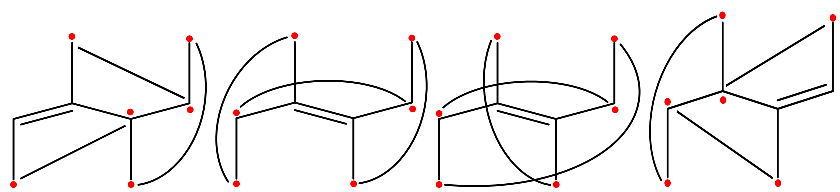

Scheme A3.2. The Rumer structures of C_8H_{10} in *R*(3) block.

$$d_{n-1} = 2^{n-2} \tag{A3.8}$$

Explanation: For cross-conjugated polyene, the short bonds of Rumer structures in *R*(n-1) block can only be found at the single bonds in *R*(0), which means that the number of Rumer structures in *R*(n-1) block is related to the number of single bonds in *R*(0) and the relationship is shown below in Table A1.

Table A3.3. The number of Rumer structures in R(n-1) block of cross-conjugated $C_{2n}H_{2n+2}$.

n	# of Rumer structures at each single bond in R(0)											sum
3					1		1					2
4				1		2		1				4
5			1		3		3		1			8
6		1		4		6		4		1		16
7	1		5		10		10		5		1	32

For C_8H_{10}, there are 3 single bonds in R(0) and each of them can form 1, 2, and 1 R(n-1) Rumer structures, So there are 4 ($2^{n-2}=2^2$) Rumer structures in R(3) block in Scheme A4.

b) QDM molecules

For *o*-QDM, represented here by the formula $C_{4n+4}H_{2n+6}$, the number of R(1) structures can be expressed as,

$$d_1 = (n+1)(n+6)(2n+1)/6 \tag{A3.9}$$

For *p*-QDM, represented here by the formula $C_{6n+2}H_{4n+4}$, the number of R(1) structures can be expressed as,

$$d_1 = 2^{n+4} - 10n - 16 \tag{A3.10}$$

These formulas lead to the values in Table A3.4.

Table A3.4. The number of R(1) Rumer structures (d_1) for QDMs.

	d_1(*o*-QDM)	d_1(*p*-QDM)
C8	7	6
C12	20	
C14		28
C16	42	
C20	75	82
C24	121	
C26		242
C28	182	
C32		668

As we can see from Table A3.4, d_1 for $R(1)$ of *p*-QDM increases much faster and will be much larger than that for *o*-QDM, so the delocalization energy will also become much larger. One can straightforwardly understand where the additional $R(1)$ structures for the *o*-QDM come from. 15 R(1) structures can be created from linear polyene C_{12}. These structures are readily retrieved as $R(1)$ structures for *o*-QDM as well, as can be seen from Table A3.5. Additionally, one $R(2)$ structures in linear C_8 is turned into a $R(1)$ in *o*-QDM C_8. An additional five $R(2)$ structures in linear C_{12} turn into R(1) in *o*-QDM C_{12}. For C_{16},

o-QDM C_{16} will have 14 $R(1)$ structures more than that for linear C_{16}. As such, one can see that for n=1, i.e. for C_8, one obtains 1 additional structure, for n=2, i.e. C_{12}, one obtains 5 additional structures (1^2+2^2), for n=3, i.e. C_{12}, one obtains 14 additional structures (1^2+2^2+3^2). As such, the additional R(1) structures for o-QDM correspond to $\sum_{i=1}^{n} i^2$

Table A3.5. R(1) for o-QDM C12. The first block corresponds to the R(1) structures which have are a direct analogue to the R(1) structures of the linear analogue; the second block corresponds to R(1) structures which correspond to R(2) structures in the linear analogue.

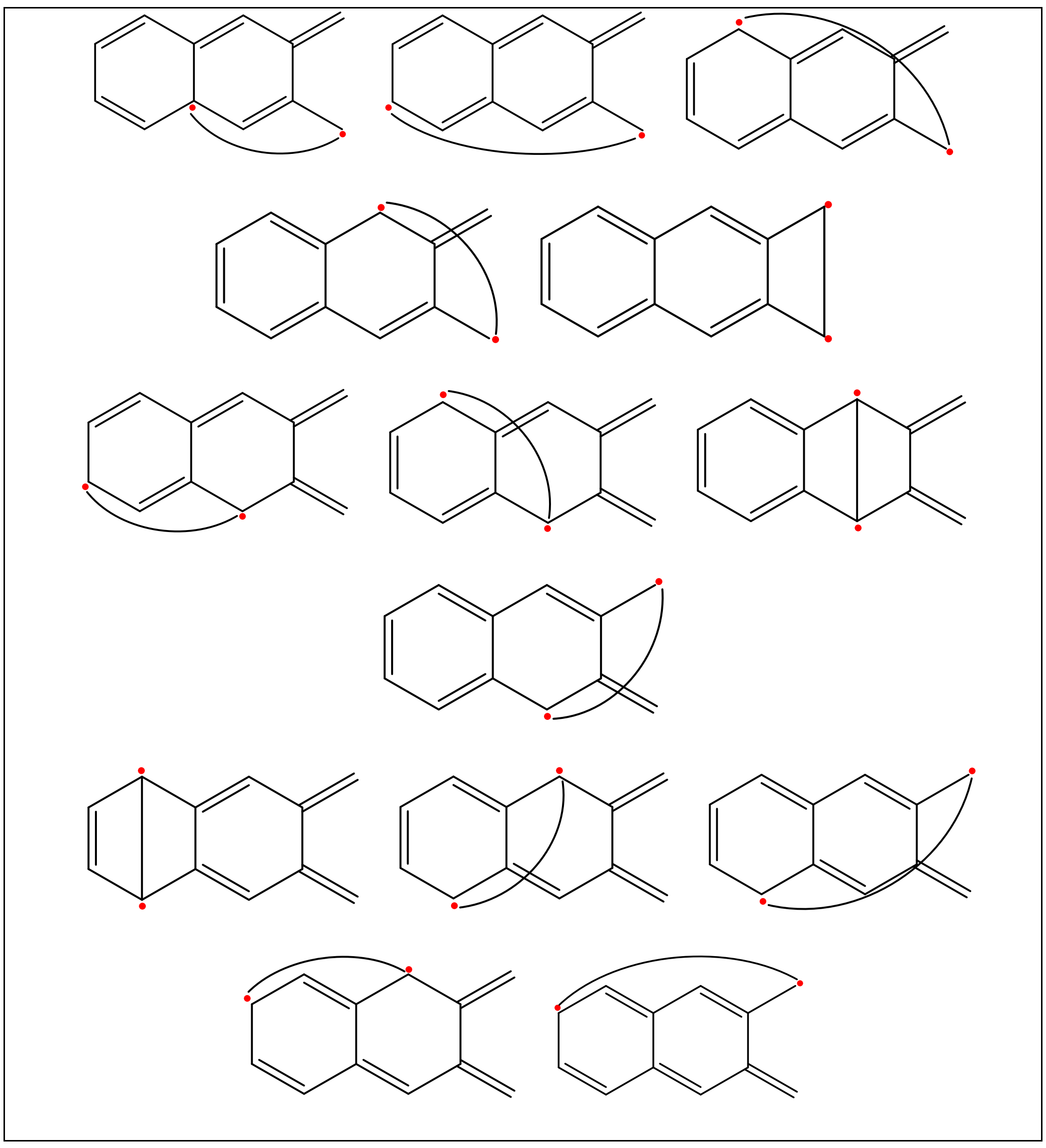

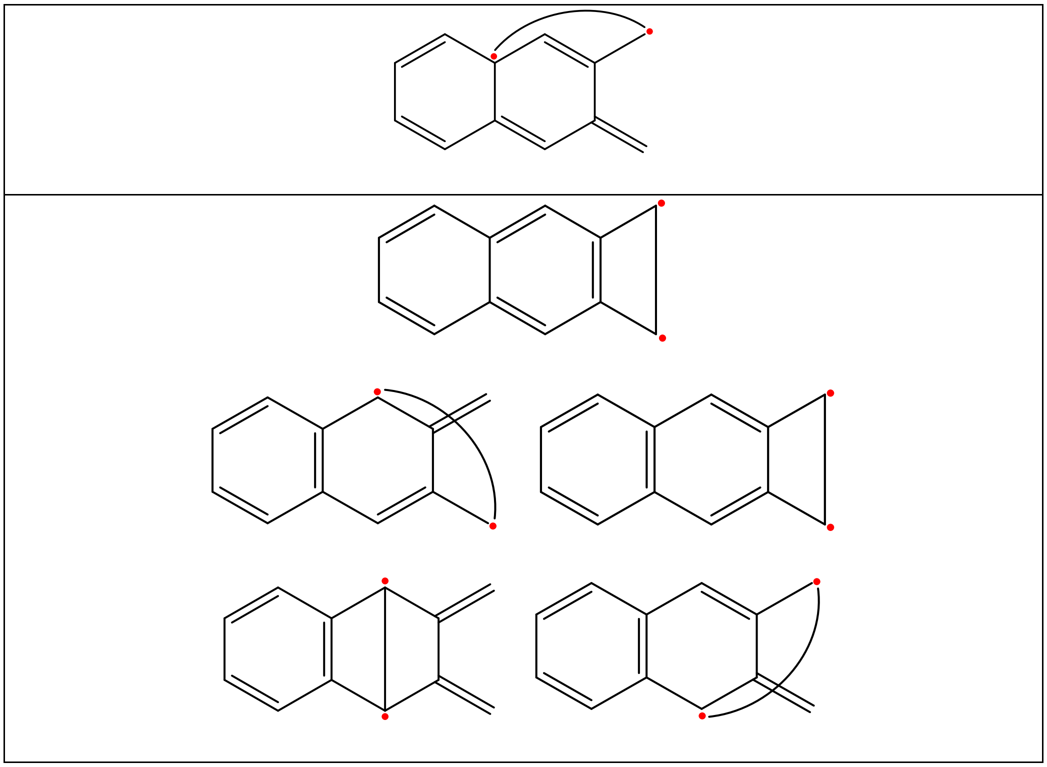

As such, one can obtain d_1 for *o*-QDMs $(C_{4n+4}H_{2n+6})$ as follows:

$$d_1 = \binom{2n+2}{2} + \sum_{i=1}^{n} i^2 \tag{A3.11}$$

This expression can be simplified to:

$$d_1 = \frac{(2n+2)(2n+1)}{2} + n(n+1)(2n+1)/6 = (n+1)(n+6)(2n+1)/6 \tag{A3.12}$$

in which the right-hand side corresponds to Eq. A3.9.

In order to derive the expression for d_1 for the *p*-QDM molecules, one should first make the following specifications: whether in the linear, cross-conjugated or QDM systems; if a pair of C=C in $R(0)$ is connected by a road with one single bond C-C or alternate singles bond and double bonds C-C=C-C, then an $R(1)$ structure can be formed. For *p*-QDM C8 in

Table A3.6, C1=C2 and C7=C8 are connected by C2-C3=C4-C7 and also C2-C5=C6-C7, so they can form two $R(1)$ with one long bond C1—C8. However, C3=C4 and C5=C6 are connected by C3-C2-C5 or C4-C7-C6, which are not alternate singles bond and double bonds, so they cannot generate any $R(1)$. C1=C2 and C3=C4 are connected only by C2-C3, which means there is only one road connecting them. As such, they form only one $R(1)$ with a single long bond C1—C4. The $R(1)$ structures for $C_{14}H_{12}$ can be found in Table A3.7.

Table A3.6. Rumer structures for *p*-QDM C_8H_8.

	***p*-QDM C8**
R（0）	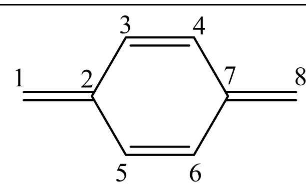
R（1）	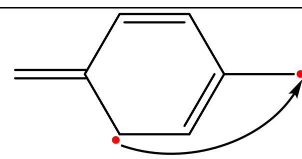 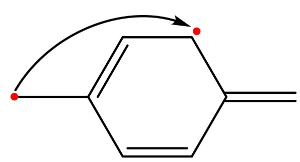 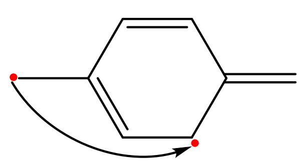 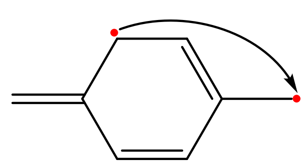

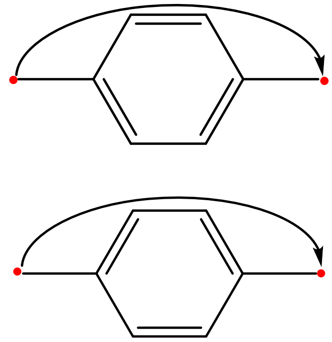

Table A3.7. R(1) for *p*-QDM C14.

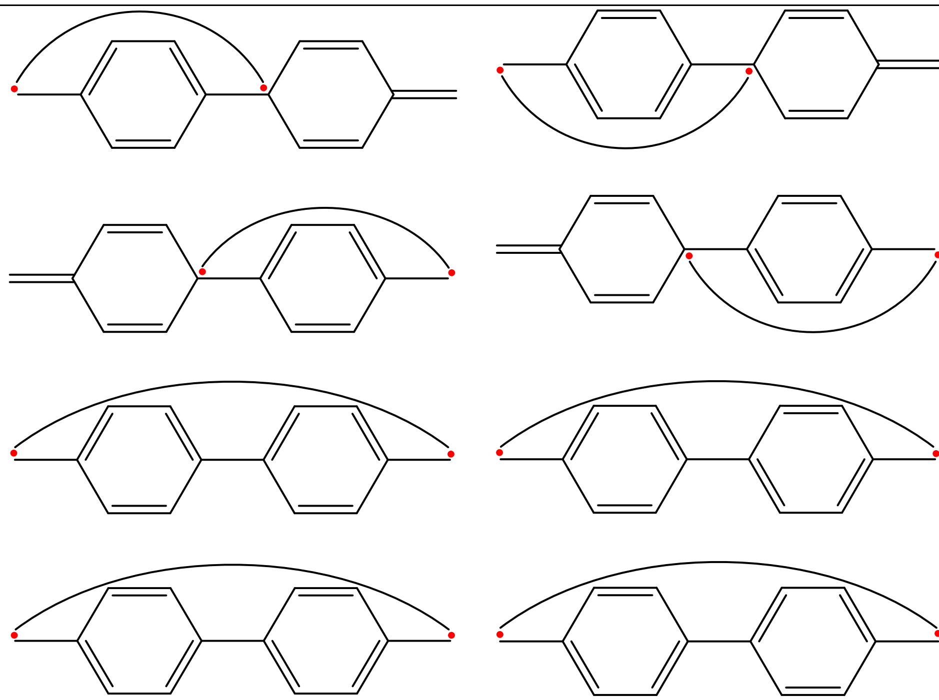

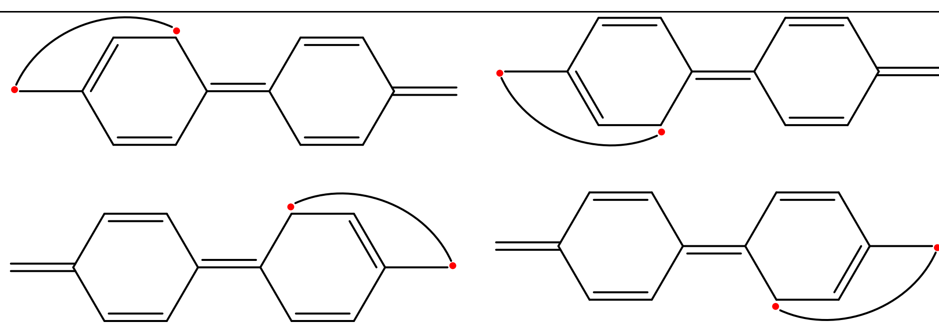

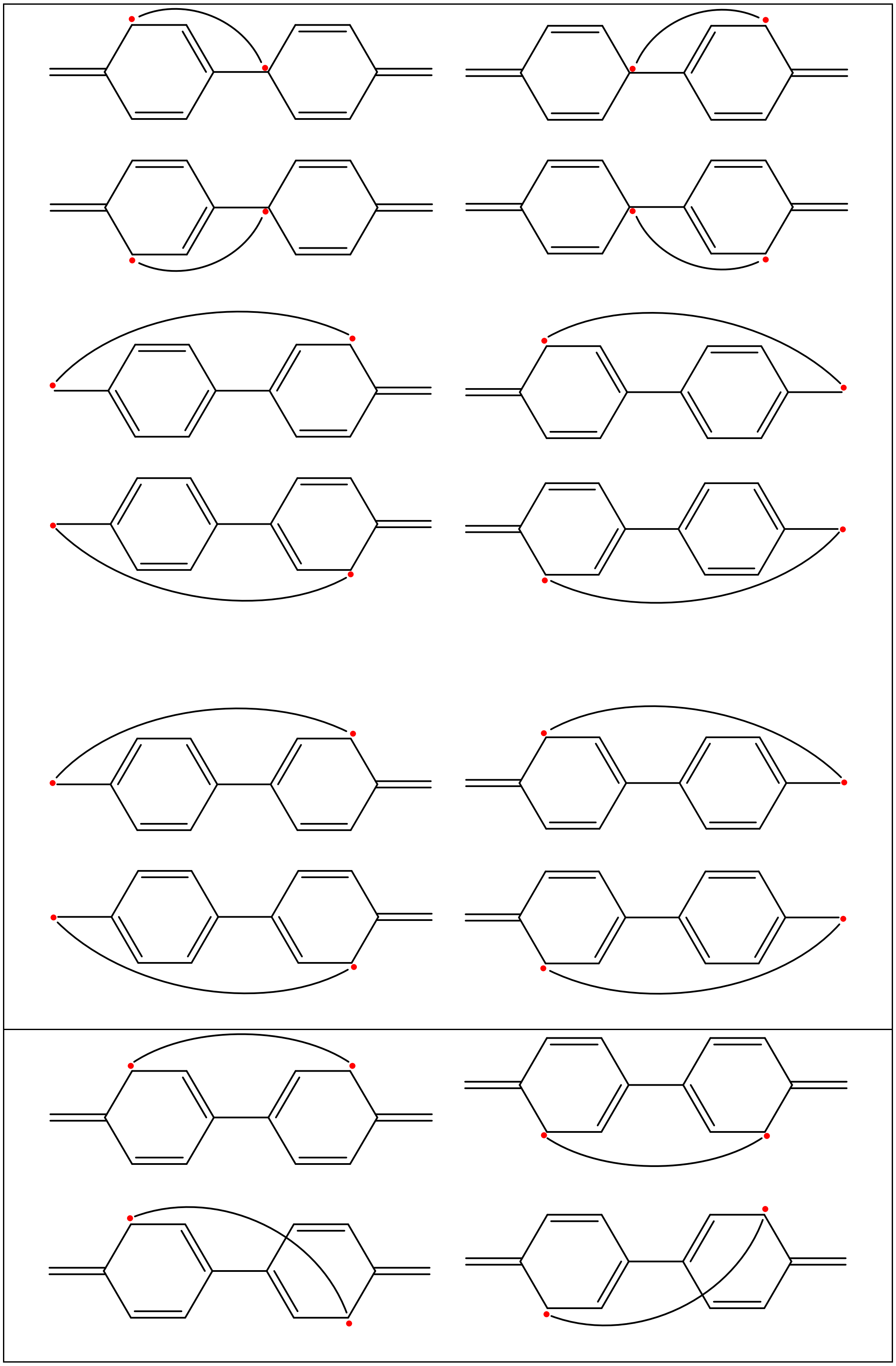

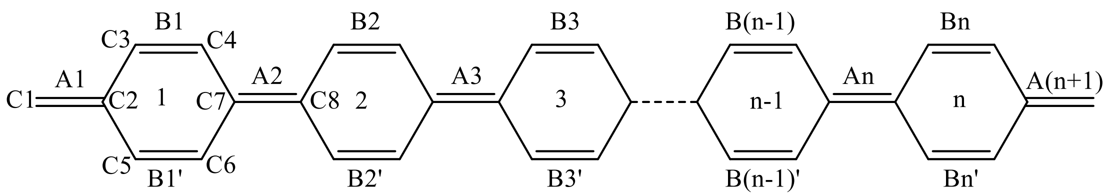

Figure A3.1. The structure of *p*-QDMs $C_{6n+2}H_{4n+4}$.

From Fig. A3.1, one can conclude that there are two types of C=C bonds in *p*-QDMs:

Type A: C=C bonds which connect the C6 rings;

Type B: C=C bonds within the C6 rings.

As such, for *p*-QDM $C_{6n+2}H_{4n+4}$, we can create *R*(1) in 3 ways:

(1) R(1) structures involving pairs of Type A bonds. Let us start by focusing on *R*(1) structures involving A_1 first. A_1 and A_2 give rise to two *R*(1) (C_1-C_2=C_3-C_4=C_7-C_8 and C_1-C_2=C_5-C_6=C_7-C_8). Additionally, 4 *R*(1) can be formed involving A_1 and A_3, 8 involving A_1 and A_4 etc. As such, one can create 2^n *R*(1) involving A_1 and A_{n+1}, leading to the following expression for the total number of *R*(1) which can be formed from A_1,

$$d_a(1) = \sum_{i=1}^{n} 2^i = 2^{n+1} - 2 \tag{A3.13}$$

A_2 can form additional *R*(1) with A_3, A_4, …,A_n, A_{n+1}, and the number of *R*(1) formed this way can be expressed as follows,

$$d_a(2) = \sum_{i=1}^{n-1} 2^i = 2^n - 2 \tag{A3.14}$$

Similarly, A_n can form 2 *R*(1) with A_{n+1}. For A_m (m=1,2,…n), d_a(m) can be expressed as

$$d_a(m) = \sum_{i=1}^{n+1-m} 2^i = 2^{n+2-m} - 2 \qquad \text{(A3.15)}$$

So the number of *R*(1) created in Way (1) will be

$$d_1(a) = \sum_{i=1}^{n} d_a(i) = 2^{n+2} - 2(n+2) \qquad \text{(A3.16)}$$

(2) *R*(1) structures involving pairs of Type B bonds. As B_1 and $B_{1'}$ are cross conjugated, only *R*(1) can be formed involving B_1 or $B_{1'}$ combined with respectively B_2, $B_{2'}$, …, $B_{n'}$. The total number of *R*(1) formed from B_1 or $B_{1'}$ is,

$$d_b(1) = \sum_{i=1}^{n-1} 2^i = 2^n - 2 \qquad \text{(A3.17)}$$

The number of *R*(1) formed from B_2 or $B_{2'}$ is

$$d_b(2) = \sum_{i=1}^{n-2} 2^i = 2^{n-1} - 2 \qquad \text{(A3.18)}$$

In the same way, the number of *R*(1) formed from B_{n-1} or $B_{n-1'}$ is

$$d_b(n-1) = 2 \qquad \text{(A3.19)}$$

So the number of *R*(1) created in Way (2) will be,

$$d_1(b) = 2 * \sum_{i=1}^{n-1} d_b(i) = 2^{n+2} - 4(n+1) \qquad \text{(A3.20)}$$

(3) *R*(1) structures involving one C=C bond of type A and one C=C bond of type B. Each

of the (n+1) C=C bonds of type A can form $R(1)$ with each of C=C bonds of type B. Thus, the number of $R(1)$ formed from A_1 and one of C=C bonds of type B is,

$$d_c(1) = \sum_{i=1}^{n} 2^i = 2^{n+2-1} - 2 + 2^1 - 2 \tag{A3.21}$$

the number of $R(1)$ formed from A_m (m=1,2,…,n) and one of C=C bonds of type B is

$$d_c(m) = \sum_{i=1}^{m-1} 2^i + \sum_{i=1}^{n-m+1} 2^i = 2^m - 2 + 2^{n+2-m} - 2 \tag{A3.22}$$

the number of $R(1)$ formed from A_{n+1} and one of C=C bonds of type B is

$$d_c(n+1) = \sum_{i=1}^{n} 2^i = 2^{n+1} - 2 \tag{A3.23}$$

So the number of $R(1)$ created in Way (3) will be,

$$d_1(c) = \sum_{i=1}^{n} d_c(i) + d_c(n+1) = 3*2^{n+1} - 4n - 6 + 2^{n+1} - 2 = 4*2^{n+1} - 4n - 8 \tag{A3.24}$$

Summing the $R(1)$ formed in the three different ways, one obtains the expression for d_1 in Eq. A3.10.

[S1] Almenningen, A.; Gatial, A.; Grace, D. S. B.; Hopf, H.; Klaeboe, P.; Lehrich, F.; Nielsen, C. J.; Powell, D. L.; Traetteberg, M. The molecular structure of 3-methylene-1, 4-pentadiene studied by gas-phase electron diffraction and by vibrational, NMR and ultraviolet spectroscopy. *Acta Chem. Scand. Ser. A.* **1988**, *42*, 634-650.

[S2] Su, P.; Jiang, Z.; Chen, Z.; Wu, W. Energy decomposition scheme based on the generalized Kohn–Sham scheme. *J. Phys. Chem. A* **2014**, *118*, 2531-2542.

[S3] Gu, J.; Wu, W.; Danovich, D.; Hoffmann, R.; Tsuji, Y.; Shaik, S. Valence bond theory reveals hidden delocalized diradical character of polyenes. *J. Am. Chem. Soc.* **2017**, *139*, 9302-9316.